Macroscopic Migration of Implanted Deuterium in Silicon

Tatsuya KATABUCHI

Macroscopic Migration of Implanted Deuterium in Silicon

Tatsuya KATABUCHI

A dissertation submitted to the Doctoral Program
in Physics, the University of Tsukuba
in partial fulfillment of the requirements for the
degree of Doctor of Philosophy (Science)

January, 1999

Abstract

We have studied the formation mechanism of the ring-like flaking in silicon implanted with deuterium ions. It is the first observations of the decrease of implanted-deuterium concentrations. The decrease of implanted-deuterium concentrations was observed above an irradiation dose of 5.4×10^{17} D/cm^2. The present observations have been made by measuring the deuterium concentration using the nuclear reaction ^{2}H(d,p)^{3}H. The dependence of a critical dose for the first flaking on several parameters has also been measured. In order to understand the surface flaking mechanism and the macroscopic migration of implanted deuterium, we have proposed a new model based on the percolation of gas bubbles. The macroscopic migration of implanted deuterium gives the most probable interpretation of the generation of the ring-like flaking pattern on the irradiated surface.

Contents

1 Introduction 3

2 Instruments 9

2.1 Ion source 9

2.2 Target chamber 9

2.3 Beam sweeping system 10

2.4 Quadrupole mass analyzer 11

2.5 Silicon solid state detector 12

2.6 Target cooling system 13

3 Experiment I:
Macroscopic migration of deuterium 14

3.1 Research technique 14

3.2 Experiments 15

3.3 Experimental results 17

4 Experiment II: Critical dose for flaking 19

4.1 Experiments 19

4.2 Experimental results 20

5 Percolation model 23

5.1 Introduction 23

5.2 Modeling 25
5.3 Macroscopic migration 27
5.4 Surface exfoliation 29

6 Discussion **34**

6.1 Macroscopic migration of implanted deuterium 34
6.2 Critical dose for flaking 36
6.3 Ring-like flaking pattern 38
6.4 Hydrogen implantation 39

7 Conclusion **41**

Acknowledgments **44**

References **45**

Tables **48**

Figures **56**

1 Introduction

We have reported observations of the ring-like flaking in Si, Ge and GaAs implanted with deuterium ions [1, 2]. Many researchers have studied the surface deformation phenomena induced by ion irradiation [3]. However, no observation of the ring-like flaking has been reported with the exception of our reports. The formation mechanism of the ring-like flaking pattern has been poorly understood. We have studied the formation mechanism of the ring-like flaking. In this paper, we report the first evidence of the macroscopic migration of implanted deuterium in silicon which generates the ring-like flaking pattern on the irradiated surface. Furthermore, in order to clarify the surface flaking mechanism, the dependence of the critical dose required for the first flaking on several parameters was also measured. In this chapter, after an overview of radiation blistering and flaking, we discuss the motivation for the present study.

When particles such as hydrogen and helium are implanted in solid at high doses, they are trapped frequently in defect complexes as gas phase. These complexes involving gas atoms or molecules are called gas bubbles. If the gas bubbles form in near-surface regions and the gas pressure is high enough, bubbles may plastically deform the surface layers above them. This phenomenon of surface deformation associated with gas bubbles formed by irradiation has been called *radiation blistering*. When the deformation is extreme, the surface layers may rupture and exfoliate. This exfoliation process has been called *flaking*.

In the early 1960's Primak et al. [4] and Kaminsky [5] first reported experimental evidence for blister formation in insulators irradiated with 100–140-keV protons and helium ions and in metals irradiated with 125-keV deuterons, respectively. Primak and Luthra [6] first observed numerous flaking craters and blisters with a diameter of 10–20 μm in silicon irradiated with 100-keV protons, using optical interferometry for surface examination. Kaminsky first reported mass spectrometric observations of gas bursts from ruptured blisters during irradiation of copper with 125-keV deuterons. After the early work by Kaminsky and Primak et al., in the 1970's, the interest in the radiation blistering phenomenon has increased greatly because of its importance in the operation of thermonuclear fusion reactors. For these reasons, mainly, the radiation blistering and flaking in metals and alloys used in the fusion reactors have been studied. However, hydrogen-induced flaking in silicon has recently attracted much attention due to an application to the shearing of macroscopic layers of silicon to make crystalline thin films [7, 8].

Models for the formation of blisters and flaking craters have been suggested by a number of authors [3]. The most plausible model is based on coalescence of microscopic gas bubbles [9]. This model consists of the following stages (Fig. 1): In the first stage, the implanted atoms and the vacancies created by irradiation agglomerate to form small (20–40 Å) gas bubbles in near-surface regions (1a–b). The next stage is the increase of the concentration of small bubbles with increasing the dose of ions, and subsequent coalescence of small bubbles leading to an internal macroscopic cavity occurs (1c–d). Finally, high gas pressure in the internal cavity induces plastic deformation and exfoliation of the surface layer (1e–f).

In 1994, we reported the first observation of the ring-like flaking in Si, Ge, and GaAs implanted with 90-keV deuterium ions [1]. Figure 2 shows a scanning electron micrograph and a schematic cross section of typical ring-like flaking in silicon. The most important feature of the ring-like flaking is that the flaking craters form a macroscopic pattern of beam-size order on the irradiated surface. No observation of a flaking phenomenon that induces such a macroscopic structure was reported, so far, although numerous small flaking craters randomly formed on the irradiated surface were observed. Features of the ring-like flaking can be summarized as follows: (1) An instantaneous eruption of deuterium gas occurs at a critical dose. (2) As a result of the intermittent eruption, one ring-like flat-bottomed crater is formed on the irradiated surface. With increasing deuterium dose, the ring-like flaking craters are formed one by one concentrically as shown in Fig.3. (3) The depth of these craters is equal to the range of the implanted deuterium ions. (4) The crater pattern is independent of the crystallographic orientation of the irradiated surface.

Recently, the spontaneous formation of the organized spatial, temporal, or spatio-temporal structures found in many physical and chemical systems has fascinated many scientists [10, 11, 12]. We are also interested in the ring-like flaking as a pattern formation phenomenon.

To understand the formation mechanism of the ring-like flaking pattern in silicon, we have speculated that the ring-like pattern could be generated by some macroscopic migration of implanted deuterium in silicon. Macroscopic movement of implanted deuterium can make a spatial pattern depending on deuterium concentrations in the irradiated area. However, implanted deuterium atoms in silicon are thought to be immobile at room temperature because most implanted deuterons may be trapped by dangling bonds of vacancies much created in the implanted region [13, 14]. Accordingly, instead of the diffusion of deuterium atoms, we have expected migration of D_2 molecules along a network of gas bubbles. If the macroscopic network of gas bubbles exists in the implanted region, the D_2 molecules in the network can move macroscopically, like a fluid soaking into a porous medium. In this study, we have developed a new method to investigate the existence of the macroscopic network along which D_2 molecules can move freely. This method is based on the measurement of decreases of deuterium concentrations caused by macroscopic migration of D_2 molecules after the formation of a flaking crater. The deuterium concentrations in the implanted layer were determined by counting protons emitted from the nuclear reaction ^{2}H(d,p)^{3}H. Using this method, we first observed the decreases of deuterium concentrations which may be induced by the macroscopic migration of D_2 molecules along the gas-bubble network.

We consider that the formation of the macroscopic network of gas bubbles must be described by percolation theory, which treats random connected networks in a disordered medium [15, 16, 17]. A percolation phenomenon is characterized by the existence of a sharp threshold of concentration above which an infinite network percolates through a system. The measured decreases of deuterium concentrations also has a threshold of deuterium dose and shows the characteristic of percolation well. In Chapter 5, we will propose a percolation model to explain the experimental results.

We have also measured the dependence of the critical dose for the first flaking on several parameters. Percolation process of gas bubbles described above occurs between stage (c) and (d) in Fig.1. With increasing deuterium dose, the macroscopic network become fatter and, at least, changes to a macroscopic gas-filled cavity as shown in (e). After formation of the cavity, high pressure in it induces plastic deformation of surface layer leading to exfoliation. The process after stage (d) is not described by a simple percolation picture. However, in order to explain the formation of the ring-like flaking pattern, a picture about the process from stage (d) to (f) is also needed. For this reason, we have measured dependence of critical dose for the first flaking on several parameters, which generally reflects the mechanism of surface deformation process after stage (d) [3]. In this study, the dependence of the critical dose on dose rate (beam intensity) and projectile energy was measured. In particular, projectile-energy dependence of the critical dose provides well information about the surface deformation process because surface layer thickness depends on projectile energy.

2 Instruments

2.1 Ion source

Experiments were performed at the University of Tsukuba. The D^- or H^- beam with energies between 30 and 100 keV was used for ion implantation and beam analysis. The ion beam was provided from a negative ion source with a charge exchange with cesium (Fig.4). At first, positive ions (D^+ or H^+) are produced by a duoplasmatron. These positive ions extracted from the duoplasmatron with an energy of about 10 keV and decelerated to an energy of 1 keV for D^+ (500 eV for H^+). The positive ions pass through cesium vapor in the charge exchange cell and then negative ions (D^- or H^-) are produced by the double charge exchange of the positive ions with cesium atoms. After the charge exchange, the negative ions are accelerated up to a bombarding energy by means of a 10-gap accelerating tube. Finally, the velocity of the D^- or H^- ions are selected with a Wien filter.

2.2 Target chamber

For the ion implantation and the analysis described in Chapter 3 and 4, we designed a rectangular solid target-chamber, which was 500 mm long, 250 mm wide and 250 mm high. Figure, 5 and 6 show the experimental setup of the target chamber. The chamber was mounted at the end of the ion source through a dipole magnet placed just after a quadrupole magnet behind the Wien filter. The dipole magnet bent the D^-(H^-) beam with an angle of 5 degrees in order to separate unwanted neutral particles D^0(H^0) produced by single charge exchange in the cesium cell since the neutral particles cannot be swept out by the Wien filter. The D^-(H^-) ions bent by the magnet bombarded a target mounted on the copper holder through a single slit. The D^0(H^0) beam was stopped at an aluminum baffle. The beam spot size was defined by the single slit. The implantation dose was measured by integrating the beam current on the target with a current integrator (ORTEC 439). Secondary electrons from the target were suppressed by an electric potential of 300 V applied on an aluminum plate just in front of the target. The pressure in the chamber was kept lower than 3×10^{-5} Pa by using a turbo-molecular pump and a liquid-nitrogen trap.

2.3 Beam sweeping system

In order to obtain uniform distribution of the beam intensity on the target, we designed a beam sweeping system. This consists of vertical and horizontal electric deflectors placed perpendicularly to the beam line (Fig.5–7). A voltage with a triangular wave form at a frequency of approximately 100 Hz was applied on each deflection plate to sweep the beam on the target with a constant sweep velocity. The triangular voltage was obtained by amplifying a triangular signal from a function generator (KENWOOD FG-273) with power operational amplifiers (APEX PA88). The block diagram of the beam sweeping system and the circuit of the amplifier for the beam sweeping system are shown in Figs.8 and 9, respectively. This system generated a triangular output up to 400 V_{p-p} for each deflection plate. The sign of electric potential on two deflection plates of a deflector was opposite each other. As a result, the maximum electric potential between the deflection plates was 400 V.

The amplitude of deflection on the target is given by the following formula,

$$A = \frac{VlL}{2dE}, \tag{1}$$

where V is voltage between the deflection plates, l is the plate length, L is the distance from the center of the deflection plate to the target, d is the distance between the plates and E is the ion energy. By substituting our condition into this formula, calculated amplitudes are shown in Table 1

2.4 Quadrupole mass analyzer

The eruption of D_2 gas accompanied by radiation flaking was detected with a quadrupole mass analyzer (BALZERS QMG 064) connected to the target chamber (Fig.10). As reported in a previous paper [1], D_2 gas release from silicon due to flaking is instantaneous and its duration is less than a few seconds. To detect the instantaneous change of D_2 gas pressure in the target chamber with high sensitivity, the output of the quadrupole mass spectrometer was recorded as a function of time by a multichannel analyzer (MCA) operated in the multichannel scaling (MCS) mode. Figure 11 shows a block diagram to record the output voltage of the quadrupole mass analyzer as a function of time. The output voltage of the QMG064 is linear for the logarithm of pressures [18]. The transfer function between MCA counts and the pressure display was needed to measure the mass-4 gas pressures during irradiation. The transfer function was provided from pressures shown on display for residual gas in the target chamber, i.e. H_2, H_2O, N_2+CO, O_2, Ar, and CO_2. The obtained functions are shown in Figs.12 and 13. The transfer function in 10^{-6} Pa range shown in Fig.14 was extrapolated from functions of 10^{-7} and 10^{-8} Pa range.

2.5 Silicon solid state detector

As will be described in Chapter 3, implanted deuterium concentrations were determined by counting protons emitted from the nuclear reaction $^2H(d,p)^3H$. In order to detect the emitted protons, a silicon solid state detector (HAMAMATSU S3584) was placed at $\theta_{lab} = 116°$ with a solid angle of 0.21 sr (Fig.15). The sensitive area of the silicon detector was 28×28 mm^2 and the thickness was 300 μm. Backscattered deuterons were stopped with an aluminum foil 15 μm thick in front of the detector. The emitted protons from the ^{2}H(d,p)^{3}H reaction, on the other hand, have high energy of approximately 3 MeV, so that they penetrate the aluminum foil and were detected with the SSD.

2.6 Target cooling system

Figure 16 shows the target holder and the target cooling system. A rise of target temperature during the implantation was prevented by cooling the target holder with a thermoelectric cooler (NIPPON BLOWER SM-03-71M). As the same time, electrical insulation between Plate B and Plate C was also provided because elements of the thermoelectric cooler were sandwiched between two ceramic plates. The heat rejected from the cooler was removed by circulating water at room temperature as shown in Fig.16. The target holder and the pipe for cooling-water were made of capper. In order to ensure electric and thermal conductivity between Plate A and a target silicon slice, the silicon slice was fixed on the Plate A with an electroconductive adhesive (FUJIKURA, DOTITE). The cooler has cooling powers of up to 18.7 W and maximum temperature differences of 70 °C. During the implantation, the target temperature was monitored with a capper-constantan thermocouple. The thermoelectric cooler was operated at a supplied current of 0.2 A. The target temperature was maintained at a temperature of approximately 25 °C.

3 Experiment I:

Macroscopic migration of deuterium

We have investigated macroscopic migration of implanted deuterium in silicon by using the nuclear reaction $^2H(d,p)^3H$. In particular, we have expected the existence of a macroscopic network of gas bubbles described in Chapter 1.

3.1 Research technique

We developed a new method to observe macroscopic migration of implanted deuterium in silicon induced by flaking. This method consists of the following steps shown in Fig. 17 schematically:

Step 1. (sample preparation): A sample was prepared by implanting 30-keV deuterium ions into silicon over an area of 4 × 10 mm^2 below a critical dose for flaking.

Step 2. (flaking): A small flaking crater at a local spot within the area irradiated in step 1 was made by using 30-keV deuterium beam with a small diameter of 0.5 mm.

Step 3. (measurement): Deuterium concentrations of flaked and no-flaked (skipping step 2) samples were measured using the nuclear reaction

$^{2}H(d,p)^{3}H$ induced by a probe beam with an energy of 100 keV. For flaked samples, the concentrations at a point 3 mm away from the flaking spot was measured.

This method was based on a consideration that implanted deuterium atoms at a distant point away from a flaking spot probably escapes through the flaking spot if deuterium atoms or molecules can move macroscopically. Hence, the macroscopic migration of deuterium could be detected from the measurement of such a decrease of the deuterium concentration after flaking. The decrease of the deuterium concentration was obtained from difference of the deuterium concentration between samples before and after flaking at the same dose. The deuterium concentrations were determined by counting protons emitted from the nuclear reaction $^{2}H(d,p)^{3}H$.

3.2 Experiments

In step 1, samples were prepared by irradiating 30 keV D^- beam into a single crystal silicon at room temperature. Doses were in the range from 1×10^{17} to 6×10^{17} D/cm^2. These doses were below a critical dose required for flaking. Target silicon slices were (100) oriented, p type with low resistivities of 0.06 - 0.12 Ω cm. The irradiation area was determined by a rectangular slit with an area of 4×10 mm^2. The beam uniformity in the irradiation area was maintained by sweeping the incident beam as described in Section

2.3. In order to check the uniformity of the deuterium concentration on the irradiated area of 4 × 10 mm^2 was measured for a sample implanted with 30-keV deuterium at a dose of 4.7×10^{17} D/cm^2. The deuterium concentration at several points in the irradiation area was measured by using the nuclear reaction $^2H(d,p)^3H$ induced by a 90-keV deuterium beam with a diameter of 0.5 mm. The measured vertical and horizontal distributions are shown in Figs.18 and 19. The non-uniformity of the implanted deuterium atoms around the beam center was approximately ± 5 %.

In step 2, a small flaking crater within the area irradiated in step 1 was made using a deuterium beam with an energy of 30-keV and a diameter of 0.5mm. A small crater with a diameter of 0.3 mm on average was formed on the irradiated surface by the flaking. The irradiation was stopped when a small flaking occurred. The critical dose required for the flaking was $6.3 \pm 0.1 \times 10^{17}$ D/cm^2. The flaking was observed by detecting an eruption of D_2 gas accompanied by the flaking with a quadrupole mass analyzer during the irradiation (see Section 2.4).

In step 3, deuterium concentrations for flaked and no-flaked samples were determined by detecting the emitted protons from the nuclear reaction $^2H(d,p)^3H$ induced by a 100-keV deuterium beam with a diameter of 1.5 mm. For flaked samples, a deuterium concentration at a point 3 mm away from the flaked spot was measured. The emitted protons from the nuclear reaction $^{2}H(d,p)^{3}H$ were detected with a silicon solid state detector at $\theta_{lab.} = 116°$ with a solid angle of 0.21 sr. The setup of the SSD is shown in Fig.15 (see Section 2.5). Typical energy spectrum of the emitted protons is shown in Fig. 20. A peak energy of the proton spectrum was 2.6 MeV. The energy spectrum was broad due to 15-μm aluminum foil interrupting backscattered deuterons from a target. Mean ranges for 100 keV and 30 keV deuterium ions in silicon are 1.1 and 0.44 μm, respectively. Hence the analysis in step 3 was performed without influence on deuterium concentrations at the implanted layer in step 1. The 100-keV deuterium ions lose energy in the surface layer and have the energy of 49 keV at the nuclear reaction with the deuterium implanted in step 1. The differential cross section for the $^{2}H(d,p)^{3}H$ reaction at $E_d = 49$ keV is 0.33 mb/sr at an angle of $\theta_{lab.} = 116°$ (Fig.21)[19].

3.3 Experimental results

Deuterium concentrations for 20 flaked samples and 10 no-flaked samples were investigated. Tables 2 and 3 show the proton yields per the integrated beam currents of 160 μC for flaked and no-flaked samples.

Figure 22 shows $^{2}H(d,p)^{3}H$ reaction yield for no-flaked samples as a function of the implanted deuterium dose. The reaction yield for no-flaked samples is found to be proportional to these doses. The yield was fit to the linear relation

$$N_p = a\Phi + b \,, \tag{2}$$

where N_p is proton yield and Φ is deuterium dose. By least-squares fitting, the parameters a and b were obtained to be $a = 4400 \pm 30$ and $b = 160 \pm 110$.

Figure 23 shows ^{2}H(d,p)^{3}H reaction yield for flaked samples as a function of the dose. The solid line obtained from no-flaked samples data is also shown in Fig.23. The reaction yield for flaked samples is in good agreement with the solid line up to a dose of 5.39×10^{17} D/cm^2 , but it deviates from the solid line above a dose of 5.39×10^{17} D/cm^2 (Fig.24). Figure 25 shows the differences of the proton yield between flaked and no-flaked samples. These differences increase sharply with increasing deuterium dose around 5.4×10^{17} D/cm^2.

Figure 26 shows pressure of mass-4 gas corresponding to D_2 gas at an occurrence of the step-2 flaking as a function of dose in step 1. There are three distinct regions. Below a dose of 5.4×10^{17} D/cm^2, the mass-4 gas pressure remains constant. Between 5.4 and 5.9×10^{17} D/cm^2, the pressure increases slowly with a deuterium dose. Above 5.9×10^{17} D/cm^2, the pressure suddenly increases. Figures 27 – 29 show the mass-4 gas pressure in the target chamber as a function of irradiation time for three distinct regions mentioned above.

4 Experiment II: Critical dose for flaking

We measured the critical dose for the first flaking in silicon implanted with deuterium ions. In particular, the dependence of the critical dose on beam intensity and projectile energy was measured. In addition, in order to investigate the dependence on a vacancy concentration, the critical dose for H^- irradiation of silicon was also measured.

4.1 Experiments

Experiments were performed by implanting D^- ions into single crystal silicon. Silicon wafers with low resistivity (0.06 -0.12 Ωcm), p-type (100) orientation, were used. Irradiation area was defined by a collimator with a diameter of 2.5 mm. The beam uniformity in the irradiation area was maintained as described in Section 2.3. The beam sweeping system can generate large electric field enough to sweep the beam within an irradiation spot of 2.5 mm in diameter (see Table 1). During the irradiation, the flaking was observed by detecting an eruption of D_2 gas accompanied by the flaking with a quadrupole mass analyzer. As described in Section 2.4, mass-4 gas pressure in the target chamber was recorded as a function of time from the beginning of the irradiation with multichannel analyzer (MCA) operated in the multichannel scaling (MCS) mode. At the same time, integrate beam current per 1 second was also recorded as a function of time with another

MCA. The critical dose for the first flaking was determined by integrating the beam charge up to a time at which the first flaking occurred (Fig.30). The beam-intensity dependence of the critical dose was measured at three beam intensities of 1.4, 2.5, and 3.4 μA for 30-keV D^- ion implantation. Projectile-energy dependence of the critical dose was measured for 30-, 45-, 60-, and 100-keV D^- ion implantation under the typical beam intensity of approximately 2.5 μA. Measurements were repeated twice for each energy. Similarly, the projectile-energy dependence of the critical dose for H^- ion implantations was also measured for the same energies as D^- ion implantations.

4.2 Experimental results

Figure 31 shows a typical mass-4 partial pressure in the target chamber as a function of irradiation time. Each peak corresponds to an eruption of D_2 gas accompanied by flaking. Background of mass-4 partial pressure was below 1×10^{-8} Pa. Mass-4 partial pressure at the first flaking was approximately 9×10^{-8} Pa. As a result of the first flaking, one circle crater with a diameter of about 1 mm was formed on the irradiated surface of each sample. The second and third flakings are also shown in Fig. 31. However the critical dose for other flakings after the first is not discussed in this section, because the formation of these flakings is complicated due to the strong correlation with beam distribution in the irradiated area.

Table 4 shows the measured critical dose for the first flaking at beam intensities of 1.8, 2.5, and 3.3 μA for 30 keV D^- ion implantation into silicon. The critical dose for the first flaking is independent on beam intensities. The average value of the critical dose is $6.02 \pm 0.05 \times 10^{17}$ D/cm^2.

Table 5 shows the measured critical doses for the first flaking for 30-, 45-, 60-, and 100-keV D^- ion implantations of silicon. Two measured values of the critical doses for each energy are in good agreement within an accuracy of 2 %. The critical dose for the first flaking increases with the deuterium energy.

For H^- implantation, one circle flaking crater with a diameter of about 1 mm was formed after the first flaking on irradiated surface of each sample with the exception of 30-keV H^- implantation. For 30-keV H^- implantation, numerous small craters with a diameter of 10 μm were randomly formed over the irradiated area. Figures 32 and 33 show the mass-2 pressure in the target chamber for implantation energies of 100 keV and 30 keV, respectively, as a function of irradiation time. Background of mass-2 pressure was approximately 1×10^{-8} Pa. Except for 30-keV H^- implantation, sharp eruptions of H_2 gas as shown in Fig.32 were observed. For 30-keV H^- ion implantation, as seen from Fig.33, the eruption of H_2 gas was unclear.

Table 6 shows the measured critical dose for the first flaking for 30-, 45-, 60-, and 100-keV H^- ion implantation. Similar to deuterium implantation, the critical dose increases with increasing hydrogen energy. The critical dose for H^- implantation is lower than that for D^- implantation at the same energy.

5 Percolation model

In this chapter, we propose a model to explain the surface flaking as the percolation of gas bubbles in the implant layer. This model predicts the existence of an infinite network of gas bubbles along which D_2 molecules can move freely.

5.1 Introduction

Percolation theory was born in formulating a simple stochastic model for situations such as a fluid soaking into a porous medium [15, 16, 17]. In this theory, a medium is defined as a regular infinite lattice and a random fraction p of sites in the lattice is occupied. A set of n-occupied sites connected by nearest-neighbor distances is called an n cluster. For small p, most occupied sites will be isolated. For p close to unity, on the other hand, most occupied sites form one infinite percolating cluster or network, corresponding to a situation that a fluid is percolating through a porous medium. There exists one sharp concentration p_c, called the percolation threshold. Thus, for $p > p_c$ one infinite network occurs, whereas for $p < p_c$ all clusters are finite. In this way, the percolation theory provides a simple picture about many critical phenomena.

The first application of the percolation theory to surface flaking or blistering phenomenon was performed by Wilson et al. [20]. Using the theory, they considered a model of the surface blistering in metals implanted with He^+ ions. They assumed that the diffusion coefficient of helium atoms depends on their concentrations and rapidly increases above the percolation threshold at which the helium atoms become infinitely connected to each other. Helium atoms are mobile along this connected chain. According to this model the critical dose for blister appearance is the dose at which the concentrations of helium reach the value for the onset of percolation. Using this model, in case of 300-keV He^+ irradiation in Nb and Pd, they showed that the critical dose C_{bl} for blister appearance should decrease with increasing flux, as observed by Verbeek and Eckstein [21]. However this model is unrealistic because it does not consider the fact that the majority of the implanted helium is in the form of bubbles at high doses.

Our model proposed in this chapter is different from the model by Wilson et al. that describes the blistering phenomenon as the percolation of implanted atoms. Our model describes the flaking phenomenon as the percolation of not implanted atoms but internal bubbles or microvoids in the implant region. The theoretical prediction of *density critical exponent* β, describing the network strength as $(p - p_c)^\beta$, will be compared with the value β derived from the experimental results.

5.2 Modeling

In general, the surface flaking is caused by plastic deformation of the top surface of a macroscopic cavity formed in the implanted region. The cavity is possibly formed by coalescence of gas bubbles in the implanted region as described in Chapter 1 (see Fig.1). Indeed, internal gas bubbles are observed in silicon implanted with hydrogen isotope ions at high doses and heavily hydrogenated amorphous silicon [22].

We here propose a model of the coalescence of gas bubbles leading to surface flaking using the percolation theory, in order to explain the flaking in silicon implanted with deuterium ions and the macroscopic migration of implanted deuterium in silicon. In this model, the situation of the implanted region in silicon is assumed as follows;

1. Small gas bubbles with a diameter of a few tens of angstroms trapping D_2 gas are randomly formed in the implant region. The gas-bubble concentrations increase with increasing implanted deuterium concentrations.
2. Neighboring gas bubbles connect each other, leading to a cluster of gas bubbles.
3. D_2 gas moves only in the gas bubbles and cannot exist in interstitial sites of silicon lattice. Thus, D_2 gas moves only along the cluster.

From the Assumption 1 of the random formation of gas bubbles, the coalescence of gas bubbles can be described by the percolation theory. The coalescence of gas bubbles should be considered as percolation in two-dimensional system. The straggling of ion distribution is too small to be infinite in comparison with the diameter of a gas-bubble. On the other hand, the beam diameter is infinite in comparison with the diameter of a gas bubble. In addition, the percolation of the gas bubbles in the implanted deuterium layer should be considered as percolation in a continuum system because discrete sites and bonds cannot be defined in this system. For such two-dimensional continuum system, a scaling theory of the percolation system predicts the percolation threshold of $p_c = 0.45$ as an area fraction of bubbles in a media [16].

When gas-bubble concentration reaches the value for the onset of percolation, an infinite network of gas bubbles exists in the implanted deuterium layer. The area of the infinite network rapidly increases with the increase of a dose above the percolation threshold. At least, the plastic deformation of a surface layer due to a high pressure in the infinite network leading to the surface flaking occurs.

5.3 Macroscopic migration

As mentioned above, when gas-bubble concentrations reach the value for the onset of percolation, one infinite network of gas bubbles exists in the implanted deuterium layer. D_2 molecules can move along the network infinitely. Accordingly, if a small flaking crater connecting between the implanted deuterium layer and vacuum like step 2 process in Fig.17 is made, D_2 gas in the infinite network flows along the network and escapes to vacuum through the crater. The macroscopic D_2 flow is driven by high pressure of D_2 gas in the network. In fact, an internal pressure as high as 10^8 Pa is reported [23]. The D_2 gas flow j is given by the following formula;

$$j = C(P_{in} - P_0) \tag{3}$$

where P_{in} is D_2 gas pressure in the network, P_0 is D_2 gas pressure of vacuum and C is conductance of infinite network of gas bubbles. D_2 gas pressure in infinite network of gas bubbles, P_{in}, decreases with time. When $P_{in} = P_0$, emission of D_2 gas stops.

The D_2 gas emission into vacuum induces the decrease of deuterium concentrations in the implanted layer. The decrease of deuterium concentration corresponds to the amount of D_2 molecules contained by the infinite network of gas bubbles, which is proportional to volume of the infinite network. Percolation theory provides volume of the infinite network as *percolation probability* P_∞. In general, the percolation probability P_∞ is defined as the probability that any site in a regular lattice belongs to the infinite network. In case of two-dimensional continuum percolation like the present situation, the P_∞ is considered to be a ratio of a network area to a media. The P_∞ behaves near percolation threshold p_c as follows

$$P_\infty \propto (p - p_c)^\beta \ , \tag{4}$$

where β is called *density critical exponent* as mentioned in Section 5.1. From this relation, the percolation probability P_∞ rapidly increases above the percolation threshold p_c. This behavior of the percolation probability P_∞ qualitatively describes our experimental results shown in Fig.25.

The scaling theory of percolation provides a quantitative analysis of experimental results even though the details of this model such as the formation mechanism of a gas bubble are unknown. According to the scaling theory, some quantities characterizing the behavior near the critical point such as the density critical exponent β are considered to be dimensional invariants. The dimensional invariants depend only on the dimensionality of the system and not on the specific lattice type. For two-dimensional percolation, theoretical value of the density critical exponent β is $5/36 = 0.1388...$ [15]. Hence, the validity of this model can be tested by comparison of the critical exponent β obtained from the experimental results in Fig.25 with the theoretical prediction.

5.4 Surface exfoliation

We here consider the process from the infinite gas bubble network to the surface exfoliation using the theory of elasticity. The infinite gas bubble network grows with a deuterium dose. At least, an unstable network is formed and rapidly changes to a macroscopic high pressure cavity. The high pressure in the macroscopic cavity causes a deformation of the top surface, leading to the surface exfoliation.

The implanted layer is under a large stress due to a high concentration of implanted deuterium. For example, for 30-keV deuterium ions in silicon at a dose of 5×10^{17} D/cm^2, the maximum deuterium concentration of 3×10^{22} D/cm^3 is estimated by a TRIM (TRansport of Ion in Matter) calculation [24]. This value corresponds to a pressure of the order of 10^8 Pa. The high pressure in the implanted layer produces a large strain energy. Whenever a gas bubble is added to the infinite network, the strain energy of the implanted layer decreases and, on the other hand, the surface energy of the gas bubble network increases. If the released strain energy is higher than the surface energy, the infinite gas bubble network would be unstable and would rapidly spread itself, leading to a macroscopic dome-shaped cavity. The condition required for the self-spreading of the infinite network is given by the equation

$$\frac{\partial}{\partial s}(W - U) = 0, \tag{5}$$

where W is the surface energy of the infinite network, U is the released strain energy and s is the size of the infinite network.

A similar model to explain the hydrogen-induced exfoliation in silicon has been proposed by Varma [25]. He also discussed the stability of gas bubbles from the strain energy and the surface energy. However, the situation treated by him was different from that treated by us. It was the surface exfoliation in silicon as a result of heating temperature up to 400 - 500 °C after hydrogen implantation at lower doses than the critical dose for flaking. Hence, he needed not to consider the network of gas bubbles. Each isolated gas-bubble becomes unstable with increasing temperature due to the anisotropy of the elastic forces and the evaporation or slow diffusion of atomic hydrogen to molecular hydrogen in the bubble. In contrast with our model, the coalescence of gas bubbles occurs not before but after the self-spreading process of the gas bubbles.

In order to investigate the stability of infinite network of gas bubbles, we calculated the released strain energy and the surface energy of the percolation network. As discussed in Section 5.2, the percolation of gas bubbles is considered to be continuum percolation in the two-dimensional system. However, since the calculation in the continuum system is difficult, the calculation is performed as percolation in the triangular lattice. Instead of a spherical gas bubble with a radius of r_0, one gas bubble is expressed as a hexagonal cylinder shown in Fig.34. The hexagonal cylinder with $2r_0$ wide and $2r_0$ high has the volume V_0 given by the equation:

$$V_0 = 3\sqrt{3}r_0^3. \tag{6}$$

If the gas bubbles do not exist in the implanted layer, the strain energy per a unit volume, F, is given by the equation [26]:

$$F = \frac{(1-\sigma)(2\sigma^2+1)}{2(1+\sigma)(1-2\sigma)}\frac{p^2}{E}, \tag{7}$$

where σ is Poisson's ratio, p is pressure in implanted layer and E is Young's modulus. The strain energy released by the gas bubble network W is roughly proportional to the volume of the network V as given by the following equation:

$$W = FV = FsV_0 = \frac{(1-\sigma)(2\sigma^2+1)}{2(1+\sigma)(1-2\sigma)}\frac{p^2}{E}N_\infty 3\sqrt{3}r_0^3\,, \tag{8}$$

where N_∞ is the size of the infinite network. The surface area of the gas bubble network S is given as the sum of top surface S_{top}, bottom surface S_{bottom} and internal surface $S_{internal}$. Accordingly, the surface energy U is given by the equation:

$$U = (S_{top} + S_{bottom} + S_{internal})\gamma = (3\sqrt{3}r_0^2 N_\infty + 2r_0^2 N_{i.s.})\gamma, \tag{9}$$

where γ is a surface energy per a unit area and $N_{i.s.}$ is number of side surfaces (bonds) of the network connecting with empty sites in triangular lattice. In order to estimate N_∞ and $N_{i.s.}$, a Monte Carlo simulation was performed in the 2000 × 2000 triangular lattice. For occupied probability p ranging from

0.1 to 0.99, the size, the perimeter and the internal surface of the largest cluster were computed. Figure 35 shows these results. For the triangular lattice, a theoretical value of the percolation threshold p_c is exactly 0.5 [16]. Taking the values of $r_0 = 10\mathring{A}$, $P_{in} = 10^8 Pa$, $E = 1.1 \times 10^{11} Pa$ [27], $\sigma \sim 0.3$ [28] and $\gamma = 1.4 J/m^2$ [29], the total energy $W - U$ was calculated from the size and the internal surface obtained by the Monte Carlo simulation. Figure 36 shows the calculated total energy. The total energy decreases with increasing p above $p = 0.72$. Hence, the self-spreading of the gas-bubble network could start. On the other hand, the infinite gas bubble network near percolation threshold $p_c = 0.5$ is stable. Thus, between 0.5 and 0.72 of p_c, the self-spreading of the infinite network cannot occur and only the macroscopic migration of D_2 molecules occurs along the infinite network. Similarly, the stable network near the percolation threshold possibly exists in the two-dimensional continuum system.

When the infinite network reaches an unstable point, at which $\frac{\partial}{\partial N_\infty}(W - U) = 0$, the infinite network rapidly spreads itself, leading to the formation of a macroscopic dome-shaped cavity. A surface skin of the macroscopic cavity is deformed by high pressure, at least, resulting in rupture and exfoliation. For an uniform pressure P_{in}, flaking occurs when the cavity radius is greater than the critical radius r_c given by the relation [26]:

$$r_c = \sqrt{\frac{4h^2\sigma_{ys}}{3(1+\nu)P_{in}}}, \tag{10}$$

where σ_{ys} is yield strength, ν is Poisson's ratio and h is the skin thickness. Substituting our condition, $P_{in} = 10^8$ Pa, $\sigma_{ys} = 2 \times 10^9$Pa [30], $\nu = 0.3$ and $h = 0.44\mu$m, into Eq.10, $r_c = 5\mu$m is obtained. The beam radius is much larger than the critical radius r_c and hence flaking occurs easily. The transition from the unstable network to flaking is a rapid runaway process due to a high pressure in gas bubbles. Consequently, the critical dose for flaking is equal to the dose required for appearance of the unstable network corresponding to $p = 0.72$ in case of the triangular lattice. The appearance of the unstable network is probably determined by implanted deuterium concentration. Indeed, as described in the Section 4, the implanted deuterium concentration at the critical dose for flaking were constant with no dependent on beam intensity and bombarding energy.

6 Discussion

6.1 Macroscopic migration of implanted deuterium

In the experiments described in Chapter 3, the decrease of deuterium concentrations induced by the small local flaking has been observed for samples implanted with deuterium ions above a dose of 5.39×10^{17} D/cm^2. The D_2 gas emission by the flaking increased with increasing the deuterium dose above 5.39×10^{17} D/cm^2. We interpret that the correlation between the decrease of deuterium concentrations and the increase of the D_2 gas emission by the flaking was induced by macroscopic migration of implanted deuterium in silicon.

Furthermore, we consider that the deuterium in the form of D_2 molecules may migrate along the macroscopic network of gas bubbles in the implanted layer which is predicted by the percolation model proposed in Chapter 5. Indeed, the measured decreases of deuterium concentrations show a characteristic of a percolation phenomenon that macroscopic transport along the infinite network occurs at concentrations above a threshold (Fig.25). As mentioned in Section 5.3, the scaling theory of percolation provides the quantitative analysis of experimental results even though the details of the model such as formation mechanisms of a gas bubble are unknown. According to the percolation model, the decrease of deuterium concentrations by the D_2

gas emission through the macroscopic network should be proportional to percolation probability P_∞ which behaves near the percolation threshold p_c as $(p-p_c)^\beta$. For two-dimensional percolation, the theoretical value of the density critical exponent β is 5/36. Hence, the validity of the model can be tested by comparison of the critical exponent β obtained from the experimental results with the theoretical prediction. Suppose that the gas-bubble concentration p is proportional to the implanted deuterium dose Φ, the decrease of deuterium concentrations, ΔN_d, is given by the following equation;

$$\Delta N_d = N_0(\Phi - \Phi_c)^\beta \tag{11}$$

where N_0 is a normalization factor and Φ_c is the dose required for the onset of the percolation of gas bubbles. Using this equation, we evaluate the density critical exponent β from the measured decrease of deuterium concentrations. In this case, the Φ_c is 5.39×10^{17} D/cm^2 because the ΔN_d rapidly increases at this dose. From a least-squares fitting, a critical exponent of $\beta = 0.104 \pm 0.025$ and a normalization factor $N_0 = 3.57 \pm 0.12 \times 10^3$ were obtained. The curve obtained from the fitting is shown in Fig.37. The obtained value of the critical exponent β is close to the scaling theory prediction for two-dimensional percolation systems, namely $\beta = 5/36 = 0.1388...$.

6.2 Critical dose for flaking

In Chapter 4, we measured the dependence of the critical dose for the first flaking on dose rate and projectile energy for deuterium implantation in silicon. The critical dose for flaking was found to be independent on dose rate and increases with an increase of the projectile energy.

The independence on dose rate indicates that deuterium trapping rate in the implanted region is considerably higher than deuterium loss by diffusion. This is consistent with the fact that the most implanted deuterium atoms are trapped by vacancies or other defects, and are immobile at room temperature [13, 14].

Using the computer program TRIM (TRansport of Ion in Matter) [24], we calculated the implanted deuterium ion distributions in silicon. For example, Figure 38 shows the TRIM calculation for 30-keV deuterium implantation in silicon. Tables 7 shows the calculations of mean range, straggling, a deuterium concentration and a vacancy concentration in the implanted region at the critical dose. The deuterium concentration in the implanted region at the critical dose is found to be almost constant over the present incident energies. The average deuterium concentration at the critical dose is $3.48 \pm 0.14 \times 10^{22}$ D/cm^3. Similarly, for hydrogen implantation in silicon, the TRIM calculations indicates that the hydrogen concentration in the implanted region at the critical dose is constant over the projectile energies (Table 8).

In general, surface deformation such as blistering and flaking occurs when a pressure in a macroscopic gas-filled cavity formed in the implanted region exceeds a critical pressure P_{def} needed to deform the surface layer (Fig.1(e)(f)). For a gas-filled cavity with a radius r and a surface thickness h, the critical pressure P_{def} can be written as

$$P_{def} = \frac{4h^2\sigma_y}{3(1+\nu)r^2} , \tag{12}$$

where σ_y and ν are yield strength and Poisson's ratio of the material. The critical pressure P_{def} needed for surface deformation increases with increasing the surface thickness h . If the internal pressure in the cavity is accumulated with a concentration of implanted deuterium atoms, the deuterium concentration needed for surface deformation should increase with increasing the surface thickness h. However the deuterium concentration at the critical dose calculated by the TRIM code indicates no-dependence on the surface thickness h. This result can be explained easily by the process from the gas-bubble network leading to the surface exfoliation discussed in Section 5.4. The infinite network of gas bubbles becomes fatter with increasing the deuterium concentration. At least, an unstable network is formed and changes to a macroscopic dome-shaped cavity containing high pressure D_2 gas by self-spreading process of the network. Finally, the high pressure in the macroscopic cavity causes a deformation of the surface layer, leading to surface exfoliation. In Section 5.4, the stability of the gas-bubble network depended on only a concentration of gas bubbles. For a percolation network in triangular lattice, the network was found to be stable up to a concentration of $p = 0.72$. In addition, the exfoliation process of the macroscopic cavity must be instantaneous because the internal pressure is considerably higher than the critical pressure needed to deform the surface layer of the macroscopic cavity of beam-size order. For example, from Eq.12, the critical pressure for a cavity with a diameter of 1 mm is only 2.7×10^3 Pa. Consequently, the critical pressure required for surface flaking is independent on the surface layer thickness.

6.3 Ring-like flaking pattern

In the present study, two important parameters of the critical dose C_m needed for macroscopic migration of implanted deuterium and the critical dose C_f needed for surface flaking have been measured. The difference between the C_m and the C_f can explain the formation of the ring-like flaking pattern. The ring-like flaking is formed when a beam has poor uniformity in irradiation area. Accordingly, the formation of the ring-like flaking pattern is explained as follows (Fig.40):

1. The deuterium concentrations at the most intense spot of a beam center exceed the concentrations required for flaking (approximately 3×10^{22} D/cm^3). Then the first flaking crater is formed at the beam center

(40a–b).

2. D_2 molecules around the first flaking crater escape to outside of the target silicon through the crater (40b). The macroscopic migration of D_2 molecules occurs in an area, in which the local dose exceeds a dose of 5.4×10^{17} D/cm^2.

3. As a result of the successive implantation after the first flaking, the second flaking occurs. Because the deuterium concentrations around the first flaking crater decrease due to the macroscopic migration of D_2 molecules, the second flaking crater is concentrically formed with a spatial interval from the first flaking crater.

According to the above explanation, a spatial interval between each flaking crater must be in inverse ratio with the gradient of the beam intensity. Accordingly, the spatial interval between each flaking crater should increase with the beam diameter since the gradient of the beam intensity roughly decreases with an increase in a beam diameter. In fact, it is observed that the interval between each flaking crater increases with a beam size (Fig.41).

6.4 Hydrogen implantation

For hydrogen implantation in silicon, the similar results to deuterium implantation were obtained with the exception of 30-keV hydrogen implantation (see Chapter 4). For only 30-keV hydrogen implantation, instead of the ring-like flaking, numerous small craters with a diameter of approximately $10\mu m$ were randomly formed over the irradiated area. Chemical properties of hydrogen and deuterium are same. Only the number of vacancies created by hydrogen implantation is different from that by deuterium implantation due to mass difference between a proton and a deuteron. A vacancy concentration of deuterium and hydrogen implantation at the first flaking obtained from TRIM calculations is shown in Figs.38 and 39. The vacancy concentration for hydrogen implantation is less than that for deuterium implantations. In addition, the vacancy concentration decreases with increasing the projectile energy. Consequently, we consider that the ring-like flaking may be difficult to be formed with decreasing a vacancy concentration.

7 Conclusion

In the present study, as a result of a local small flaking in silicon implanted with deuterium ions, the decrease of implanted-deuterium concentrations at a distant point away from the flaking crater have been first observed. The decrease were found to occur above a dose of 5.39×10^{17} D/cm^2. The observations were made by measuring the deuterium concentrations using the nuclear reaction ^{2}H(d,p)^{3}H. In addition, using a quadrupole mass analyzer, an emission of D_2 gas accompanied by the flaking was found to increase above a dose of 5.39×10^{17} D/cm^2.

We have proposed a new model based on the percolation of gas bubbles to explain the decrease of the deuterium concentrations. In this model, the decrease of the deuterium concentrations is induced by macroscopic migration of D_2 molecules along a macroscopic network of gas bubbles. According to this model, the decrease of the deuterium concentrations should behave as $(\Phi - \Phi_c)^\beta$, where Φ is the deuterium dose, Φ_c is a dose for onset of the macroscopic migration and β is the density critical exponent. The density critical exponent β has been estimated from the experimental results. The estimated value of the critical exponent $\beta = 0.104 \pm 0.025$ is close to the theoretical prediction for two-dimensional systems, namely, $\beta = 5/36 = 0.1388\ldots$. Hence, we conclude that the decrease of the implanted-deuterium concentrations must be induced by the macroscopic migration of D_2 molecules along the network of gas bubbles.

We have also measured the dependence of the critical dose for the first flaking on dose rate (beam intensity) and projectile energy. The critical dose was measured by detecting an instantaneous eruption of D_2-gas at the first flaking with a quadrupole mass analyzer during irradiation. The critical dose was independent on beam intensities and increased with increasing the projectile energy. The TRIM calculations indicate that the concentration of implanted deuterium in the implanted region at the measured critical doses is constant value of $3.48 \pm 0.14 \times 10^{22}$ D/cm^3 because a straggling of the implanted deuterium increases with increasing the projectile energy.

In order to understand a process from the macroscopic network of gas bubbles to the surface exfoliation, we considered stability of the network as balance between the strain energy and the surface energy of the network. Instead of a continuum system, for the network of hexagonal-cylinder cells in a triangular lattice, we calculated the strain energy and the surface energy using the Monte Carlo method. As a result of the calculation, the network was unstable above a concentration of $p = 0.72$. This result indicates that the stability of the network depends on only the bubble concentration. It is consistent with the fact that the deuterium concentration at the critical dose for the first flaking is a constant value.

Finally, we have explained the formation of the ring-like flaking, qualitatively, from the macroscopic migration of implanted deuterium.

Acknowledgments

I would like to express my profound gratitude to Associate Prof. Y. Tagishi for his guidance, many suggestions and discussions. I would like to thank Prof. K. Furuno, Prof. S. M. Lee, Associate Prof. Y. Aoki and Assistant Prof. I. Arai for the many useful comments and encouragement. I wish to acknowledge the grateful thanks to Dr. M. Tamura for reading of the manuscript and for the useful suggestions. I would like to express my gratitude to Prof. H. Kudo for the channeling analysis and for many suggestions and discussions. I would like to thank Prof. K. Murakami for the useful suggestions. I am thankful to Mr. Kawachi for his strong help in performing the experiments and valuable discussions. I would like to thank Mr. Y. Yamato for his strong support in operating the ion source. I gratefully acknowledge helpful discussions with all member of our group. I am indebted to technical staffs of the Tandem Accelerator Center for their support.

References

[1] Y. Tagishi and T. Katabuchi, Phys. Lett. **A195**, 99 (1994)

[2] Y. Tagishi, T. Katabuchi et al., in Proceedings of the Ninth International Conference on Ion Beam Modification of Materials, Canberra, February 1995, p837

[3] M. Kaminsky, in *Radiation Effects on Solid Surfaces*, edited by M. Kaminsky, Advances in Chemistry Series vol 158 (American Chemical Society, Washington, D. C., 1976)

[4] W. Primak, Y. Dayal, and E. Edwards, J. Appl. Phys. **34**, 827 (1963)

[5] M. Kaminsky, Adv. Mass Spetrom. **3**, 69 (1963)

[6] W. Primak and J. Luthra, J. Appl. Phys. **37**, 2287 (1966)

[7] M. Bruel, El. Lett. **31**, 1201 (1995)

[8] T. Abe et al. Ohyo Butsuri, **66**, 1220 (1997), [in Japanese]

[9] R. S. Blewer and J. K. Maurin, J. Nucl. Mater. **44**, 260 (1972)

[10] H. Haken, *Synergetics — An Introduction*, (Springer-Verlag, Berlin Heidelberg, 1978)

[11] G. Nicolis and I. Prigogine, *Self Organization in Nonequilibrium Systems*, (Wiley, New York, 1977)

[12] Y. Kuramoto et al., *Pattern Formation* (Asakura, Tokyo, 1995), [in Japanese]

[13] S. Muto, S. Takeda and M. Hirata, Mat. Sci. Forum **196-201** 1171 (1995)

[14] G. F. Cerofolini et al., Phys. Rev. B**41** 12607 (1990)

[15] D. Stauffer, *Introduction to Percolation Theory*, (Taylor & Francis, London and Philadelphia, 1985)

[16] T. Odagaki, *Introduction to Percolation Physics*, (Shokabo, Tokyo, 1993), [in Japanese]

[17] V. K. S. Shante and S. Kirkpatrick, Adv. Phys. **20**, 325 (1971)

[18] Operating Instructions Manual of partial and total pressure gauge BALZERS QMG 064

[19] R. E. Brown and N. Jamie, Phys. Rev. C**41**, 1391 (1990)

[20] W. D. Wilson, C. L. Bisson and D. E. Amos, J. Nucl. Mat. **53**, 154 (1974)

[21] H. Verbeek and W. Eckstein, *Appl. Ion Beams Met. Int. Conf.* 597(1974)

[22] S. J. Jeng, G. S. Oehrlein, and G. J. Scilla, Appl. Phys. Lett. **53**, 1735 (1988)

[23] L. Meda et al. Nucl. Instrum. Methods B **39**, 381 (1989)

[24] J. Biersack and J. F. Ziegler, TRIM89, version–5.1 (1989)

[25] C. M. Varma, Appl. Phys. Lett. **71**, 15 (1997)

[26] *Theory of Elasticity* L. D. Landau and E. M. Lifshitz (Tokyo Tosho, Tokyo, 1972) [Japanese version]

[27] *American Institute of Physics Handbook*; coodinating editor, D. E. Gray (McGraw-Hill, New York, 1972)

[28] W. A. Brantley, J. Appl. Phys., **44**, 534 (1973)

[29] J. N. Israelachvili, *Intermolecular and Surface Forces* (Academic Press, London, 1992)

[30] *Processing of Semiconductors*, edited by K. A. Jackson, Materials Science and Technology: A Comprehensive Treatment Vol.16 (Weinheim, New York, 1996)

List of Tables

1 Calculations of deflection amplitudes on the target at a supplied voltage of 400 V_{p-p} 50

2 Proton yield for flaked samples 51

3 Proton yield for no-flaked samples 52

4 Beam intensity dependence of critical doses for flaking in silicon implanted with deuterium ions 53

5 Energy dependence of critical doses for flaking in silicon implanted with deuterium ions 54

6 Energy dependence of critical dose for flaking in silicon implanted with hydrogen ions 55

7 Critical dose for flaking and TRIM calculations for deuterium implantation into silicon 56

8 Critical dose for flaking and TRIM calculations for hydrogen implantation into silicon 56

E_d (keV)	A_x (mm)	A_y (mm)
100	4.5	5.7
60	7.5	9.5
45	10.0	12.7
30	15.1	19.1

Table 1: Calculations of deflection amplitudes on the target at a supplied voltage of 400 V_{p-p}

Sample #	Dose (10^{17} D/cm^2)	Yield (counts)	Difference (counts)	Stat. Error
1	1.56	6708	328.5	82
2	3.13	13623	293.4	117
3	3.91	17670	-313.7	133
4	4.92	21182	645.9	146
5	5.16	22509	350.5	150
6	5.20	22748	318.5	151
7	5.38	21684	2138.8	147
8	5.39	23661	230.8	154
9	5.39	21503	2388.9	147
10	5.39	22257	1634.9	149
11	5.47	23648	587.3	154
12	5.47	21586	2649.3	147
13	5.51	21378	3029.8	146
14	5.59	21822	2929.6	148
15	5.63	22184	2739.5	149
16	5.63	21558	3365.3	147
17	5.86	22371	3584.6	150
18	5.91	22514	3648.2	150
19	5.94	22831	3468.1	151
20	5.94	23603	2696.7	154

Table 2: Proton yield for flaked samples

Sample #	Dose (10^{17} D/cm^2)	Yield (counts)	Stat. Error
1	1.56	7034	84
2	2.34	10364	104
3	3.09	13926	118
4	3.13	13903	119
5	4.69	20803	144
6	4.69	20661	144
7	4.69	20765	147
8	4.69	20790	147
9	4.69	20735	144
10	4.69	20737	147
11	4.69	21025.0	144

Table 3: Proton yield for no-flaked samples

Beam Intensity		Critical dose
(μA)	(10^{14} D/cm^2 sec)	(10^{17} D/cm^2)
3.3	4.2	5.94
2.5	3.2	6.05
1.4	1.8	6.06
average		6.02 ± 0.05

Table 4: Beam intensity dependence of critical doses for flaking in silicon implanted with deuterium ions

Sample #	Energy (keV)	Critical dose (10^{17} D/cm^2)	Beam intensity (μA)
1	100	7.10	2.8
2	100	7.23	1.3
average		7.16	
3	60	6.73	2.8
4	60	6.78	2.9
average		6.76	
5	45	6.13	2.6
6	45	6.22	2.6
average		6.18	
7	30	5.75	2.3
8	30	5.59	2.2
average		5.67	

Table 5: Energy dependence of critical doses for flaking in silicon implanted with deuterium ions

Sample #	Energy (keV)	Critical dose (10^{17} H/cm^2)	Beam intensity (μA)
1	100	4.23	2.6
2	100	4.41	1.3
average		4.32	
3	60	3.87	2.6
4	60	3.86	2.4
average		3.87	
5	45	3.61	3.0
6	45	3.67	2.9
average		3.64	
7	30	3.24	2.4
8	30	3.26	2.3
average		3.25	

Table 6: Energy dependence of critical dose for flaking in silicon implanted with hydrogen ions

	Measurement	TRIM calculation			
E_d (keV)	Critical dose (10^{17} D/cm^2)	Range (μm)	Straggling (μm)	Ion density (10^{22} D/cm^3)	Vacancy density (10^{22} /cm^3)
100	7.16	1.08	0.15	3.60	106
60	6.76	0.75	0.14	3.63	105
45	6.18	0.60	0.13	3.31	99.5
30	5.67	0.44	0.12	3.39	85.0

Table 7: Critical dose for flaking and TRIM calculations for deuterium implantation into silicon

	Measurement	TRIM calculation			
E_p (keV)	Critical dose (10^{17} H/cm^2)	Range (μm)	Straggling (μm)	Ion density (10^{22} H/cm^3)	Vacancy density (10^{22} /cm^3)
100	4.32	0.88	0.11	3.00	35.0
60	3.87	0.59	0.098	2.96	34.1
45	3.64	0.47	0.092	2.97	32.5
30	3.25	0.35	0.083	3.28	30.0

Table 8: Critical dose for flaking and TRIM calculations for hydrogen implantation into silicon

List of Figures

1 Schematics of formation mechanism of blister and flaking crater [3] 60

2 A SEM picture (above) and schematic cross section (below) of the ring-like flaking crater in Si implanted with 90-keV deuterium ions 61

3 Evolution of the ring-like flaking pattern. Beam energy: 90 keV, beam diameter: 3 mm. 62

4 A schematic view of the negative ion source 63

5 A top view of the experimental setup 64

6 A side view of the experimental setup 65

7 A schematic view of the electric deflector 66

8 A block diagram of the beam sweeping system 67

9 A circuit diagram of the amplifier 68

10 Setup of the quadrupole mass analyzer 69

11 A block diagram of the quadrupole mass analyzer 70

12 Transfer function between MCA counts and the pressure display of QMG064 in 10^{-7} Pa range 71

13 Transfer function between MCA counts and the pressure display of QMG064 in 10^{-8} Pa range 72

14 Transfer function between MCA counts and the pressure display of QMG064 in 10^{-6} Pa range 73
15 Setup of the SSD 74
16 A schematic view of the cooling system 75
17 Experiment I: experimental procedure 76
18 Vertical distribution of implanted deuterium atoms 77
19 Horizontal distribution of implanted deuterium atoms 78
20 Energy spectrum of the emitted protons from the nuclear reaction ^{2}H(d,p)^{3}H 79
21 Differential cross section for the nuclear reaction ^{2}H(d,p)^{3}H at an angle of $\theta_{lab} = 116°$ [19] 80
22 Proton yield for no-flaked samples 81
23 Proton yield for flaked samples 82
24 Proton yield in the dose range above 4×10^{17} D/cm^2 for flaked samples 83
25 Difference of proton yields between flaked and no-flaked samples 84
26 Mass-4 gas partial pressure at the step-2 flaking 85
27 Mass-4 gas partial pressure at flaking for a sample of an implantation dose of 5.9×10^{17} D/cm^2 86
28 Mass-4 gas partial pressure at flaking for a sample of an implantation dose of 5.4×10^{17} D/cm^2 87

29 Mass-4 gas partial pressure at flaking for a sample of an implantation dose of 1.6×10^{17} D/cm^2 88
30 Experimental II: Experimental procedure 89
31 Mass-4 gas pressure for 60-keV D^- irradiation of silicon . . . 90
32 Mass-2 gas pressure for 100-keV H^- irradiation of silicon . . . 91
33 Mass-2 gas pressure for 30-keV H^- irradiation of silicon . . . 92
34 A hexagonal cylinder and a triangular lattice 93
35 Calculation of 2000 × 2000 triangular lattice 94
36 Total energy of triangular lattice 95
37 A fitting result (solid curve) and difference of proton yields between flaked samples and no-flaked samples 96
38 TRIM calculation for 30-keV deuterium implantation into silicon 97
39 TRIM calculation for 30-kev hydrogen implantation into silicon 98
40 Schematics of formation mechanism of the ring-like flaking craters 99
41 Optical micrographs of the ring-like flaking for various beam sizes. The beam diameter of (a), (b), (c) and (d) is 0.5, 1, 2 and 4 mm, respectively. 100

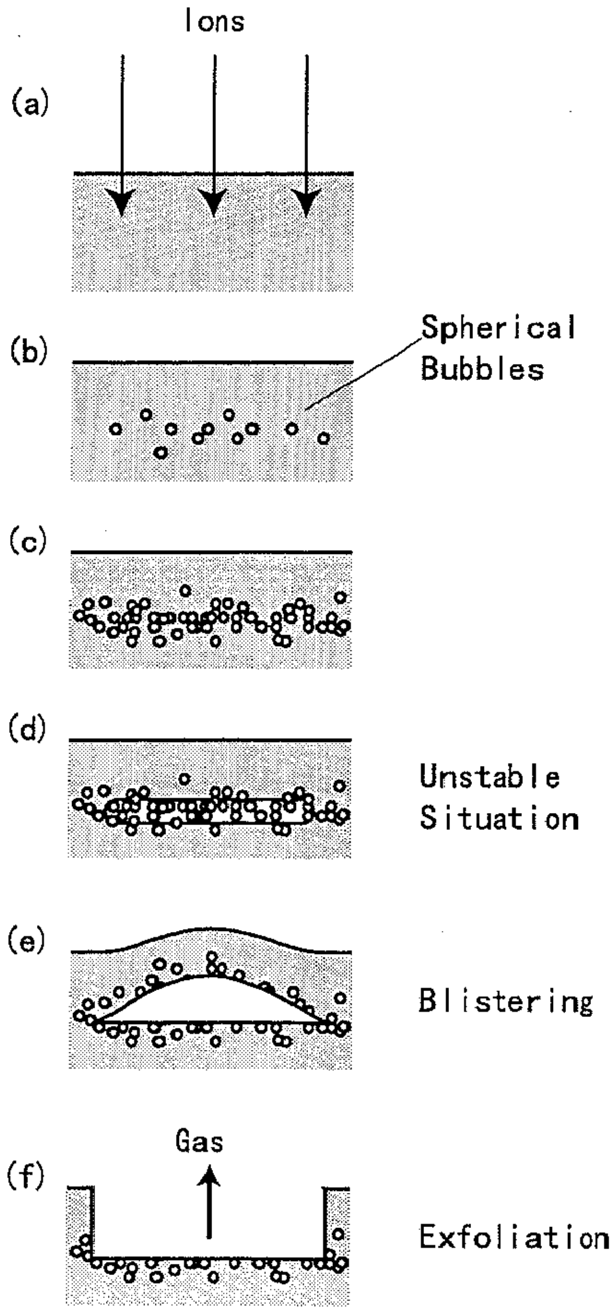

Figure 1: Schematics of formation mechanism of blister and flaking crater [3]

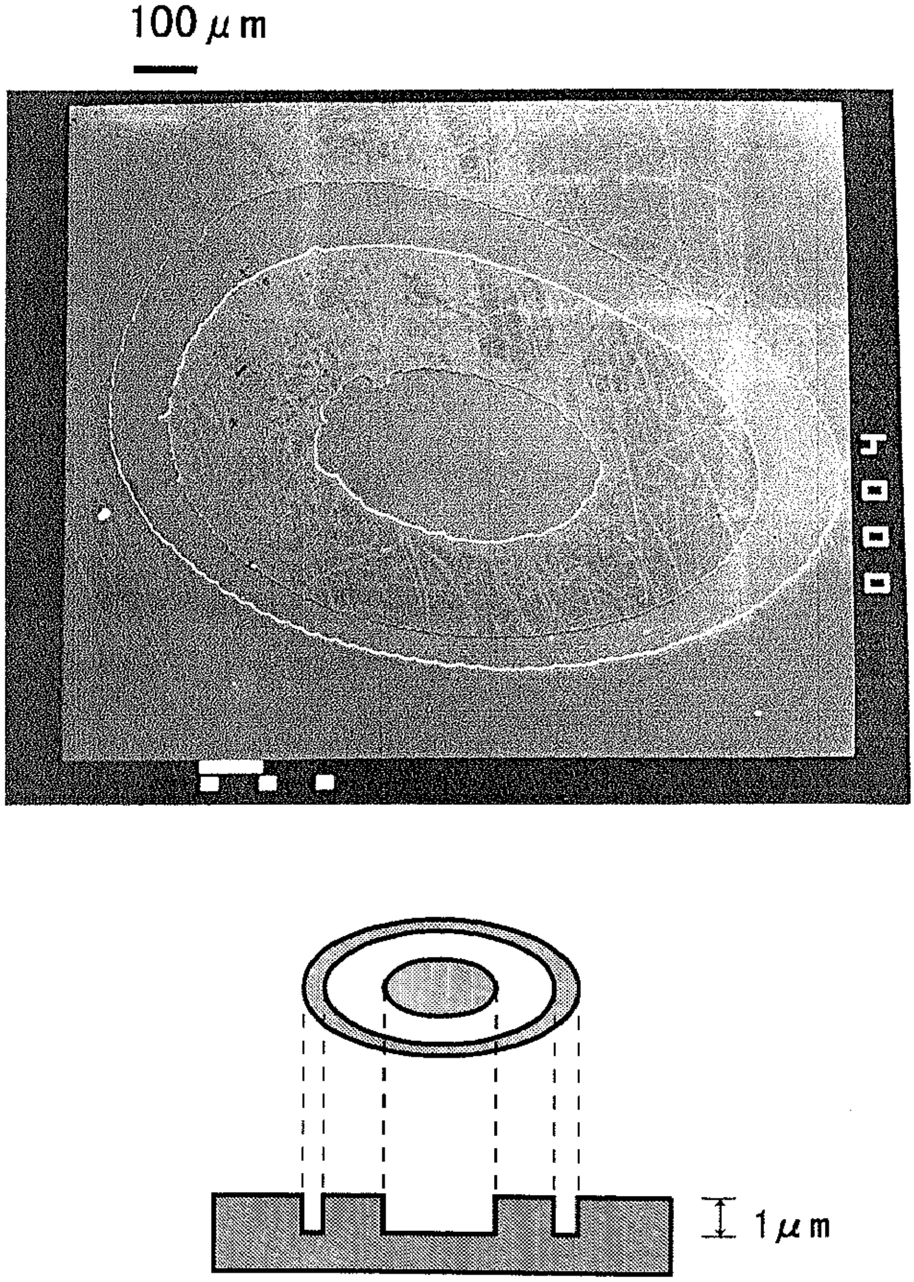

Figure 2: A SEM picture (above) and schematic cross section (below) of the ring-like flaking crater in Si implanted with 90-keV deuterium ions

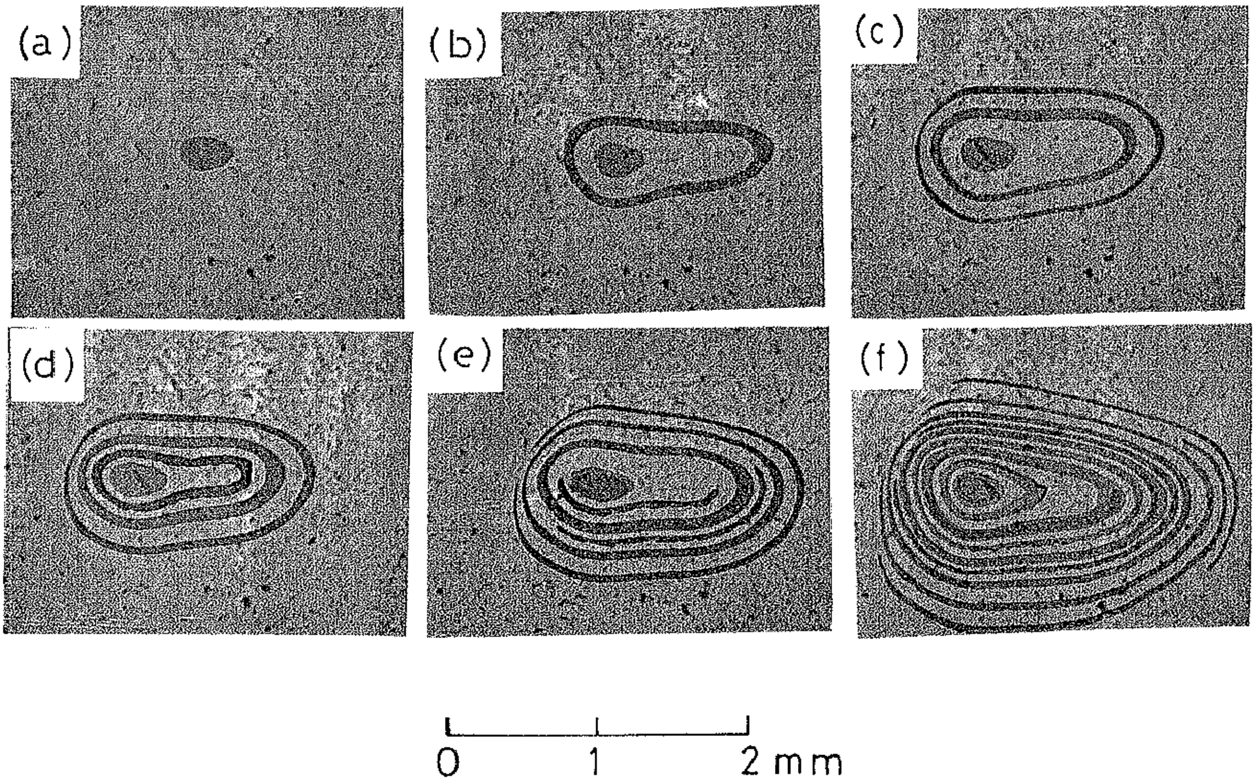

Figure 3: Evolution of the ring-like flaking pattern. Beam energy: 90 keV, beam diameter: 3 mm.

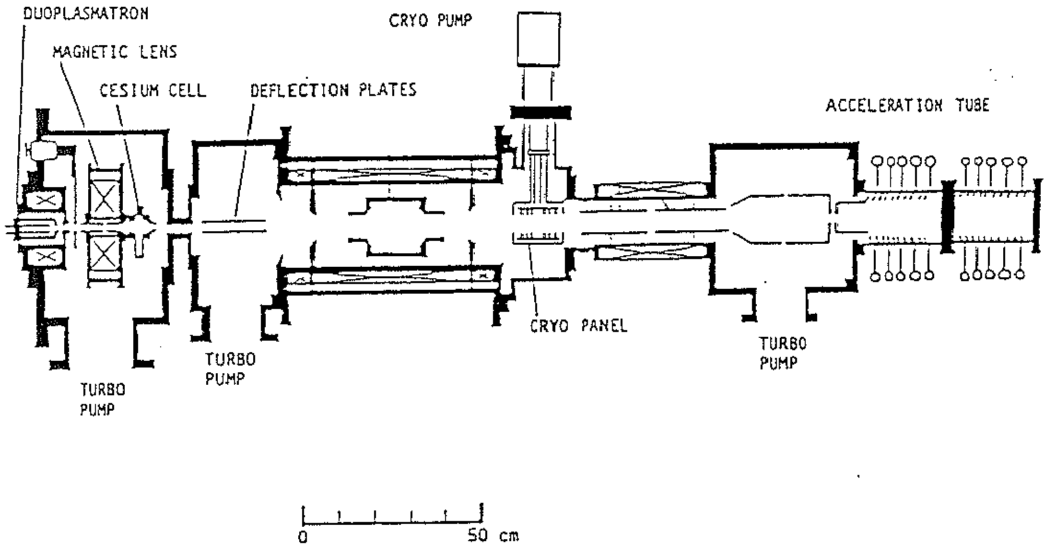

Figure 4: A schematic view of the negative ion source

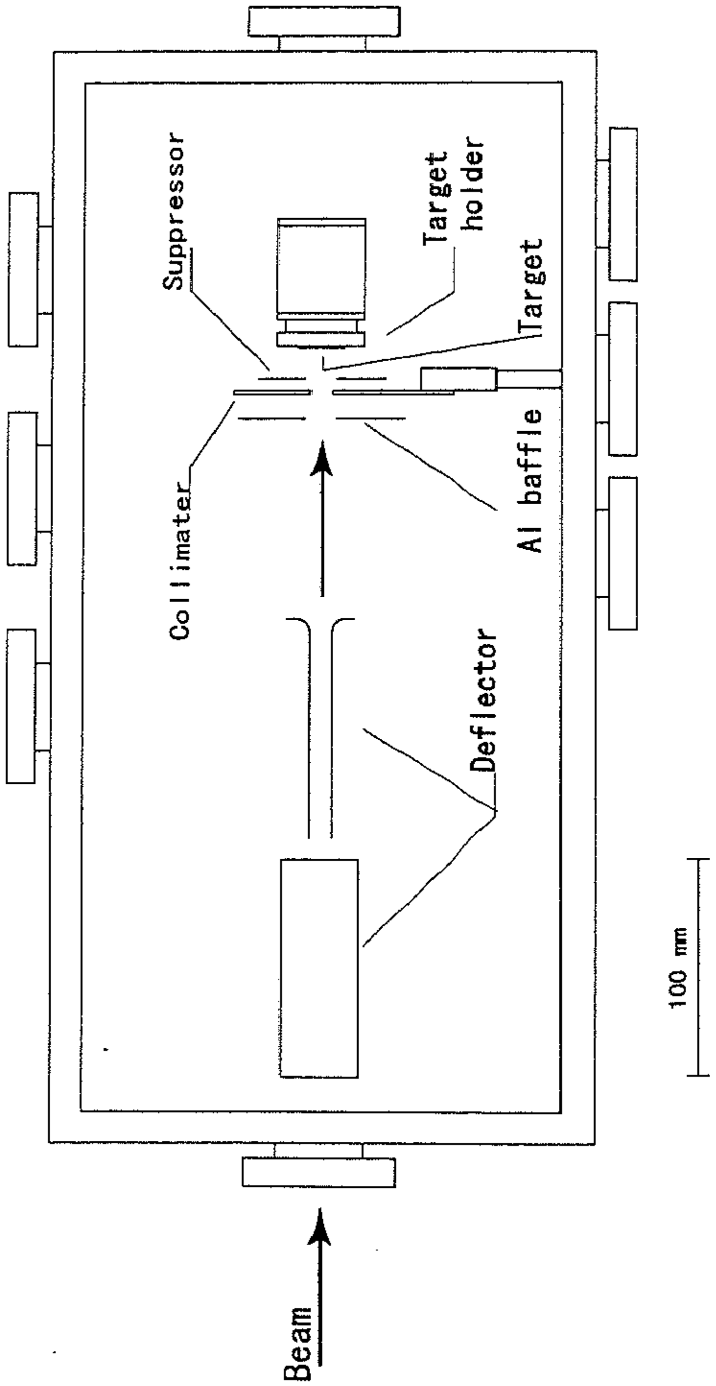

Figure 5: A top view of the experimental setup

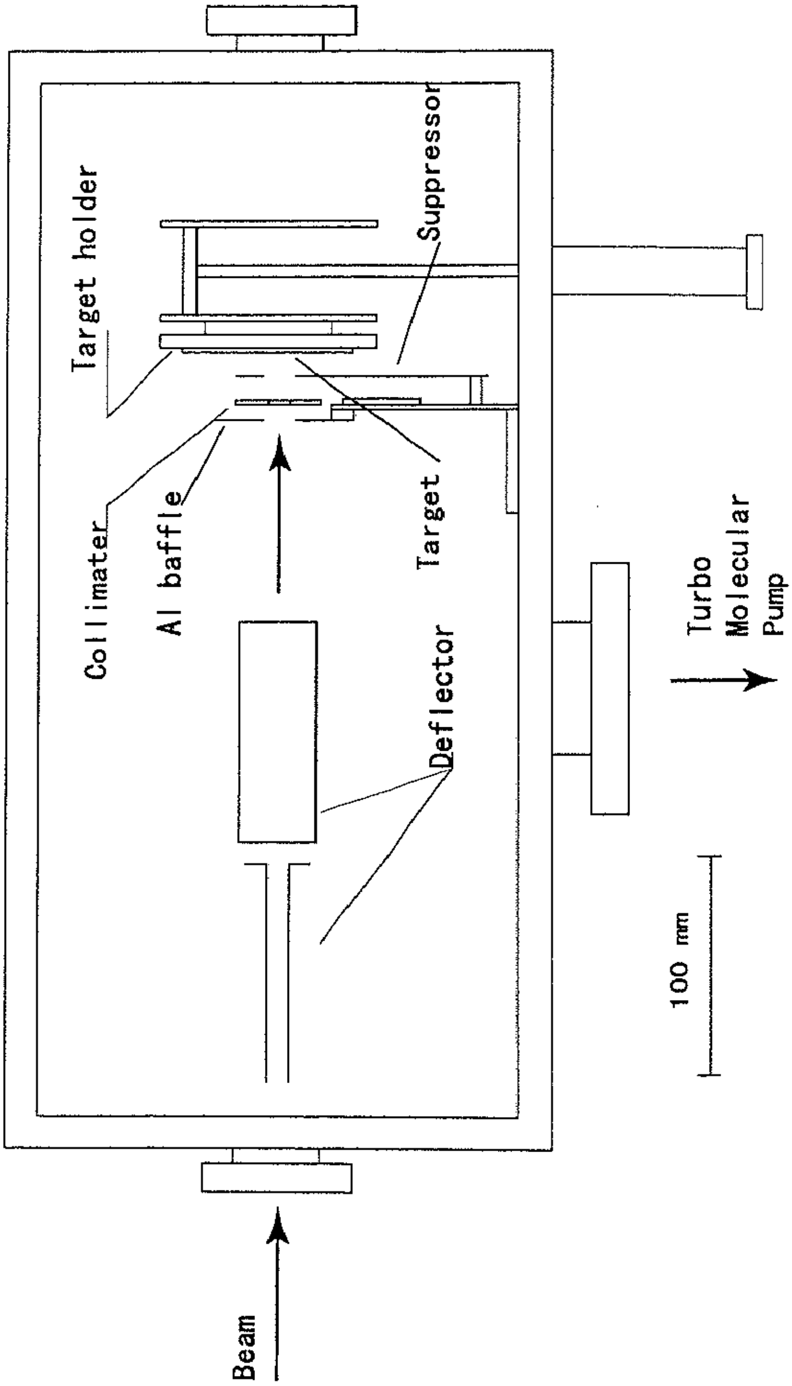

Figure 6: A side view of the experimental setup

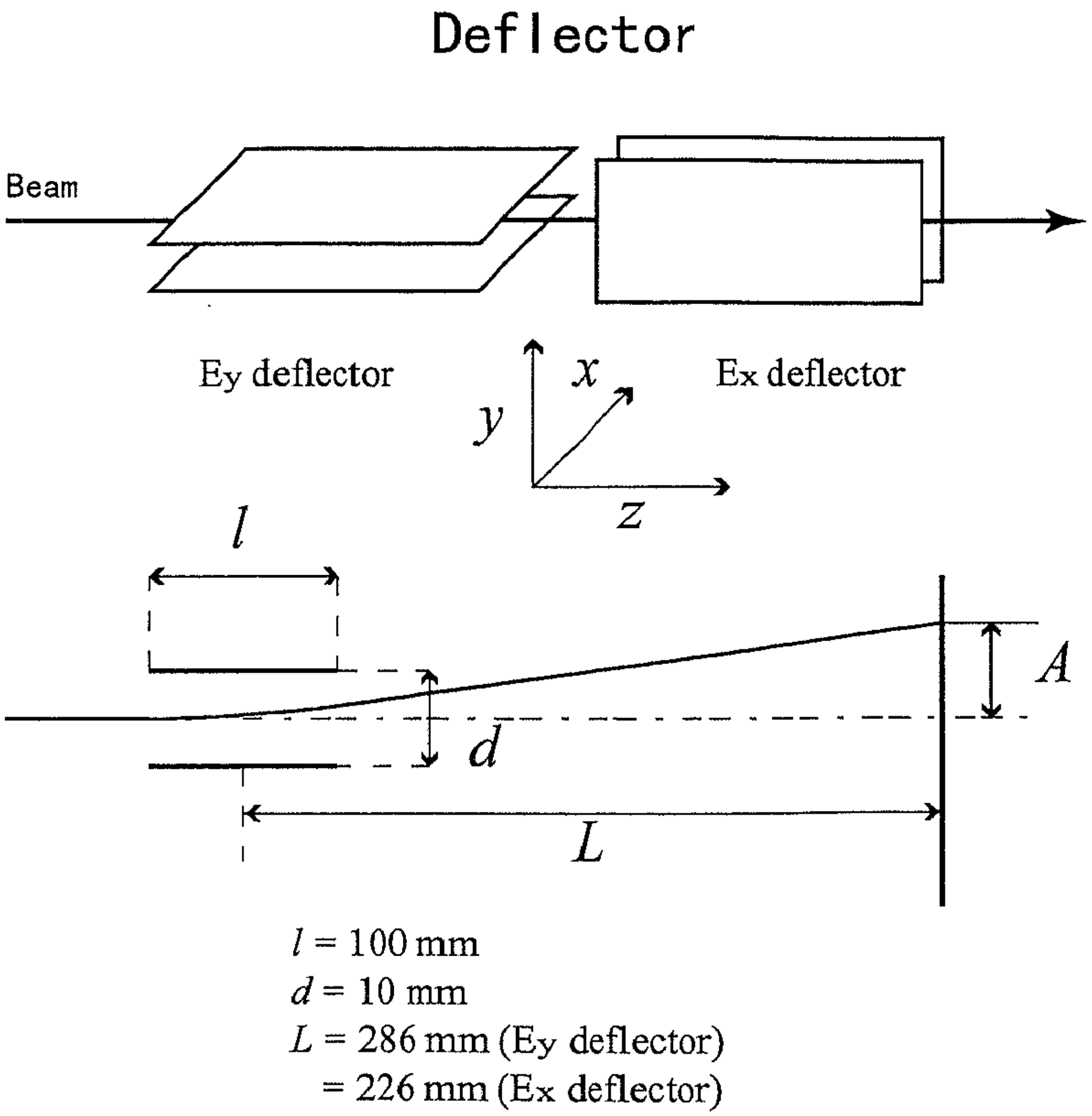

Figure 7: A schematic view of the electric deflector

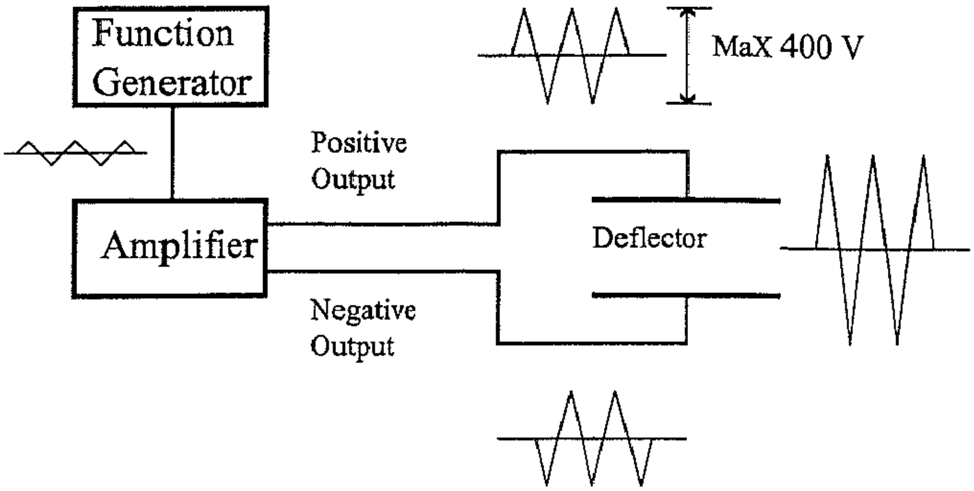

Figure 8: A block diagram of the beam sweeping system

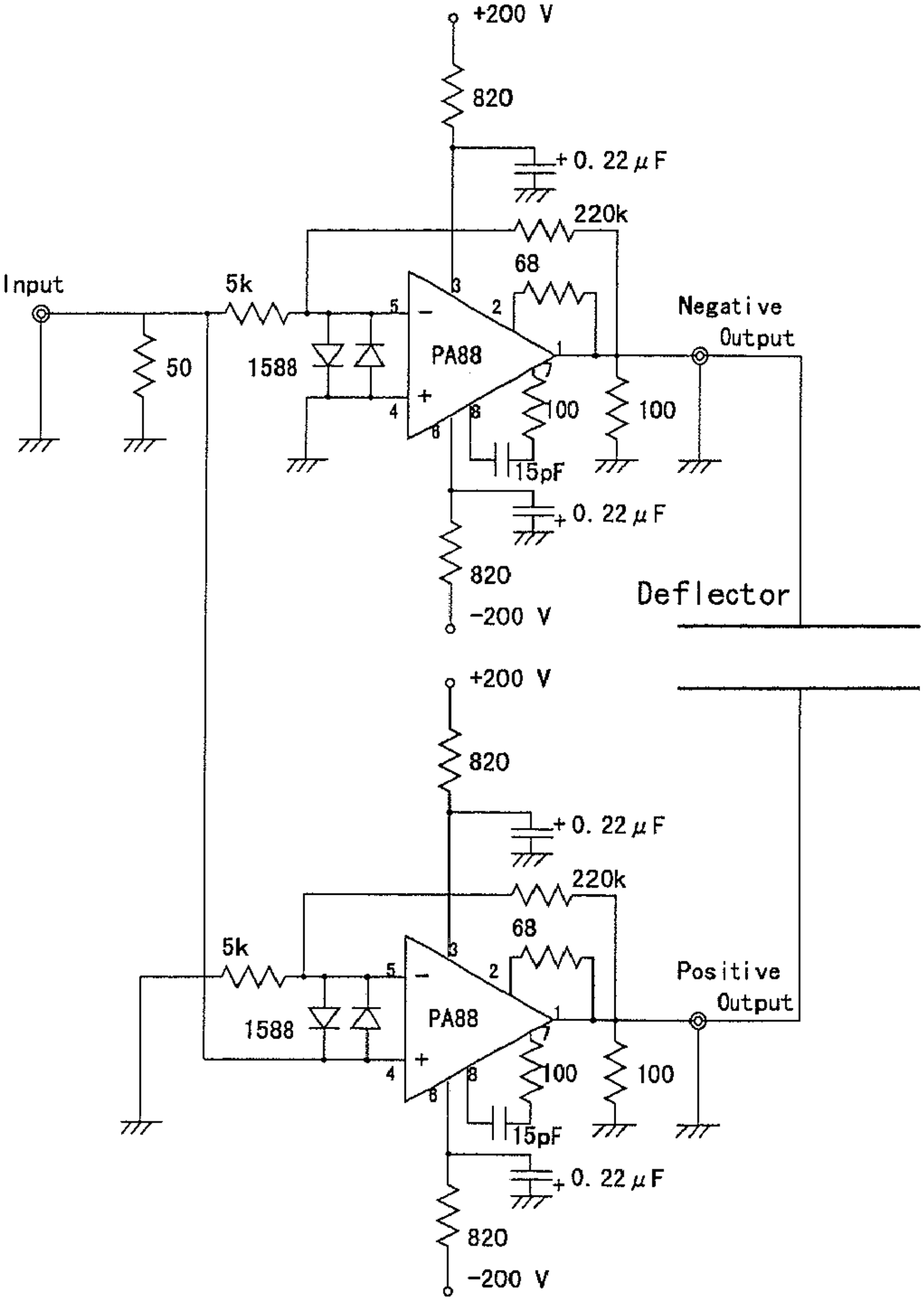

Figure 9: A circuit diagram of the amplifier

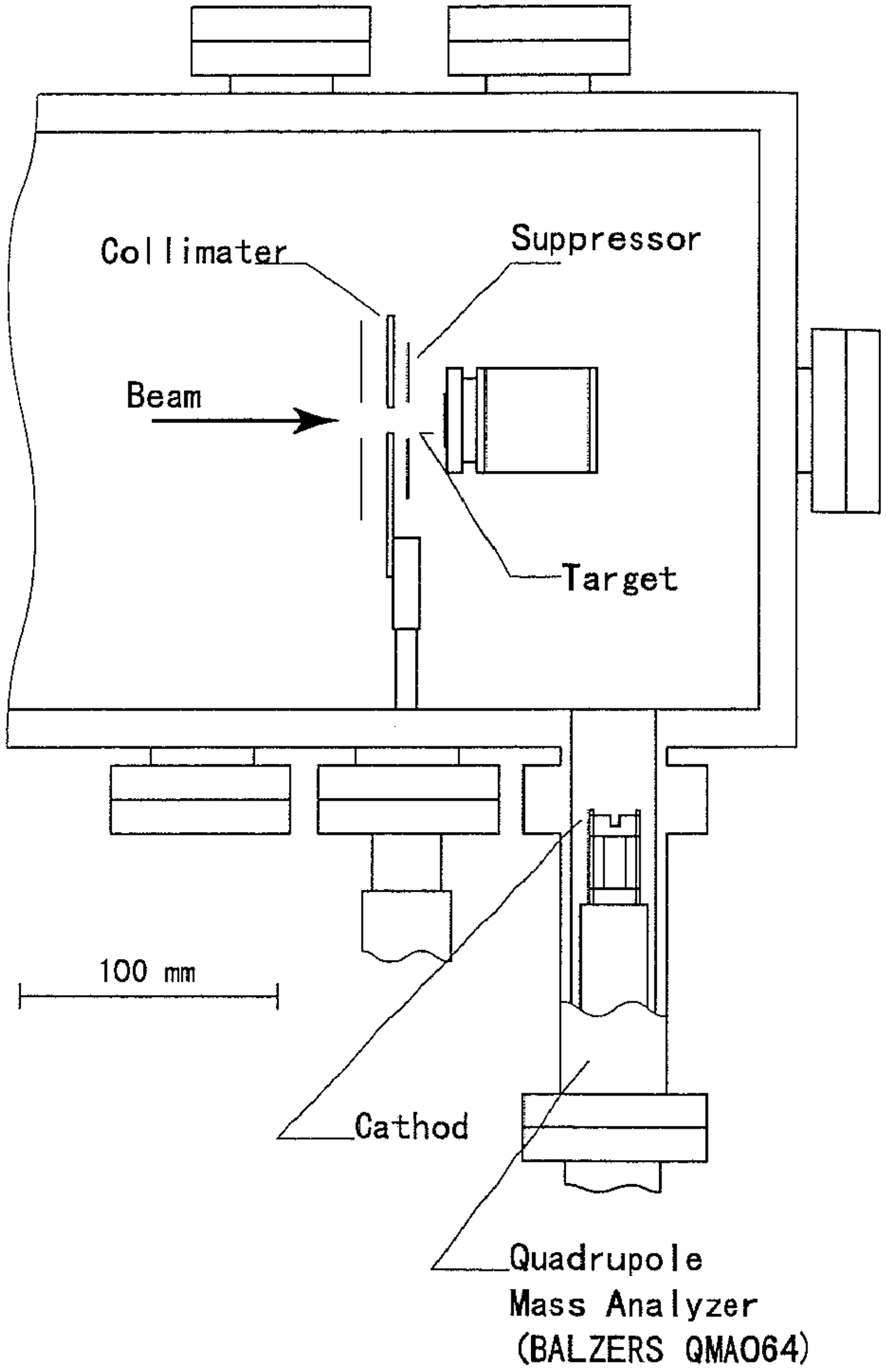

Figure 10: Setup of the quadrupole mass analyzer

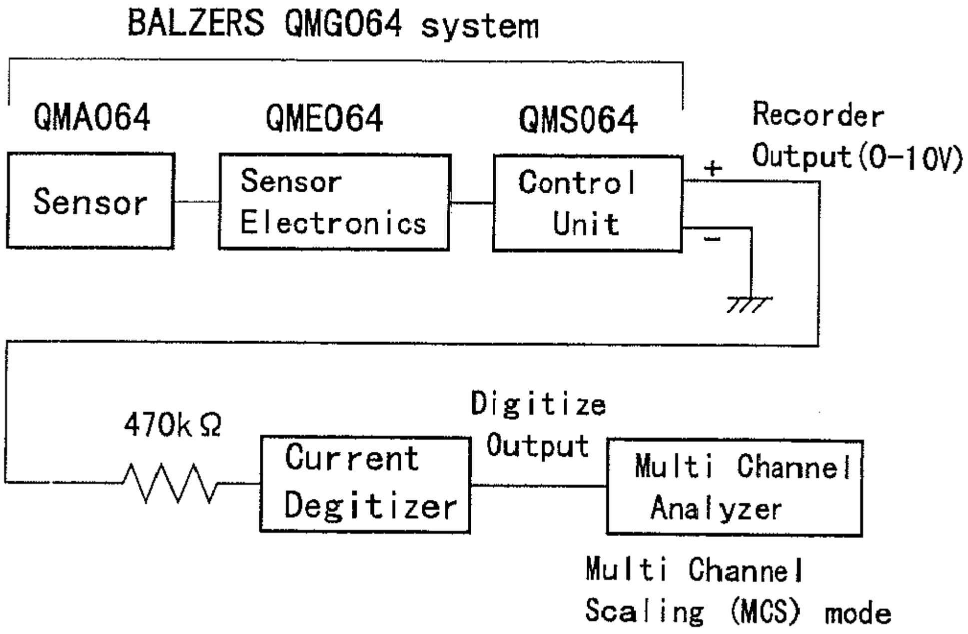

Figure 11: A block diagram of the quadrupole mass analyzer

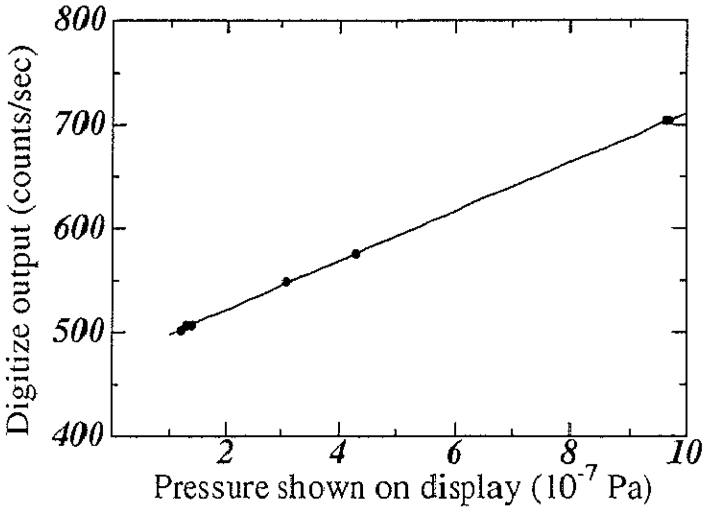

Figure 12: Transfer function between MCA counts and the pressure display of QMG064 in 10^{-7} Pa range

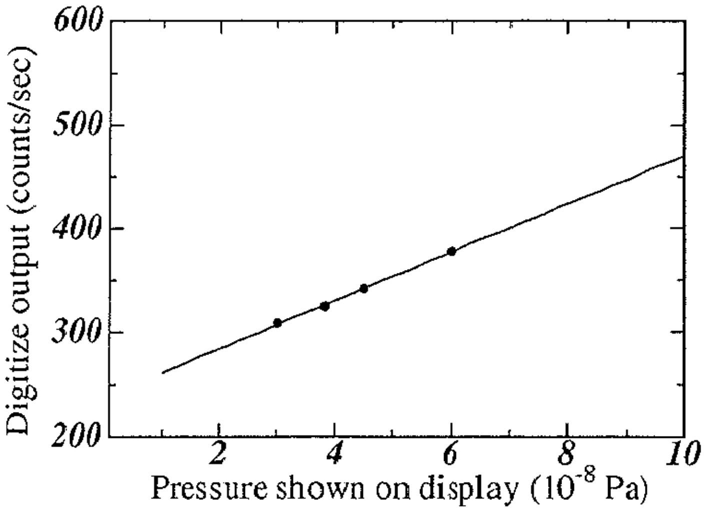

Figure 13: Transfer function between MCA counts and the pressure display of QMG064 in 10^{-8} Pa range

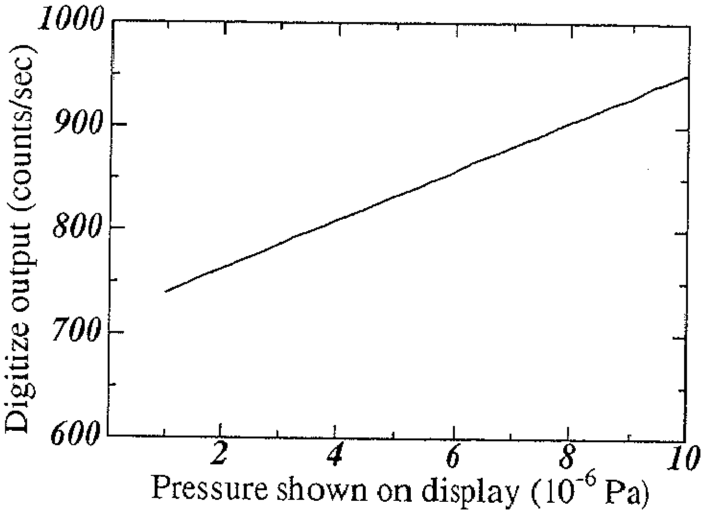

Figure 14: Transfer function between MCA counts and the pressure display of QMG064 in 10^{-6} Pa range

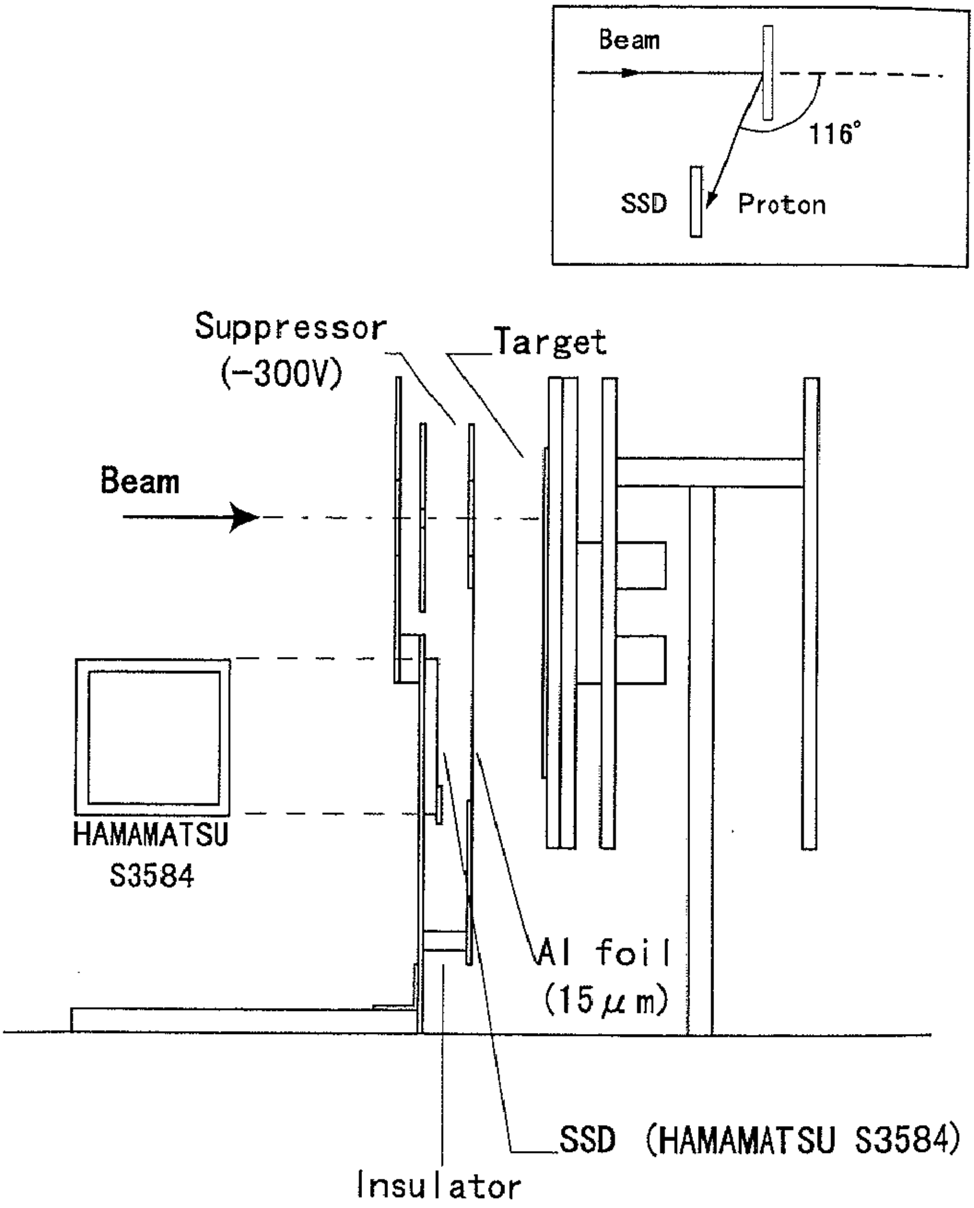

Figure 15: Setup of the SSD

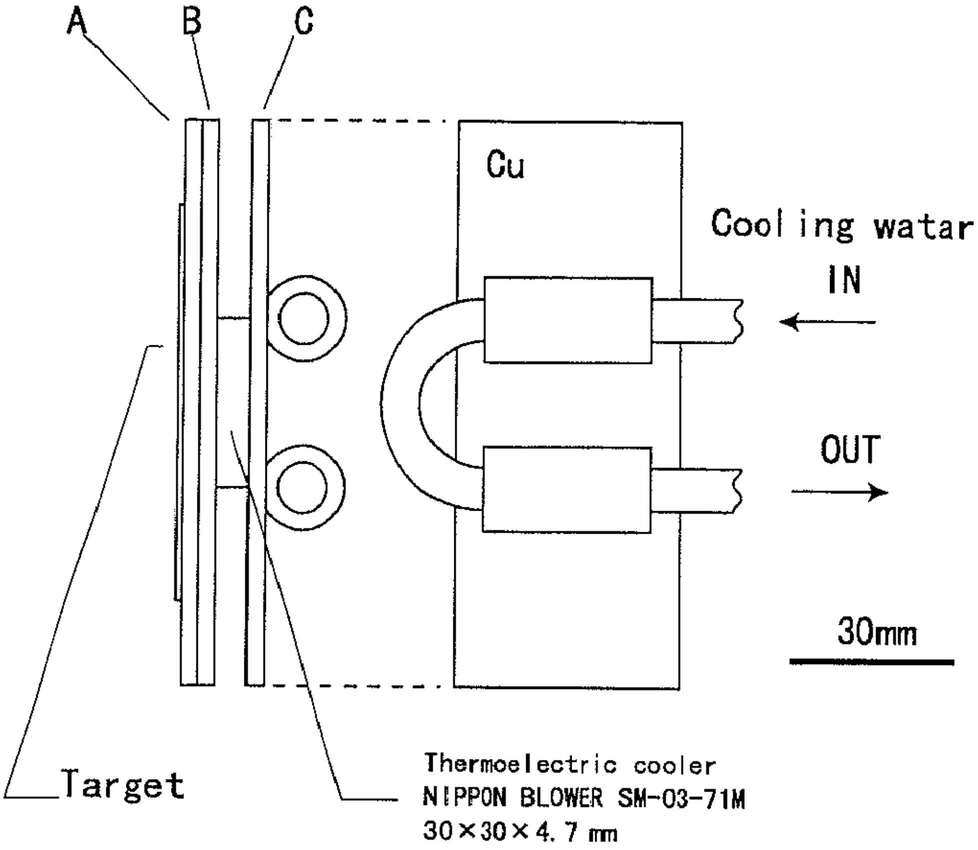

Figure 16: A schematic view of the cooling system

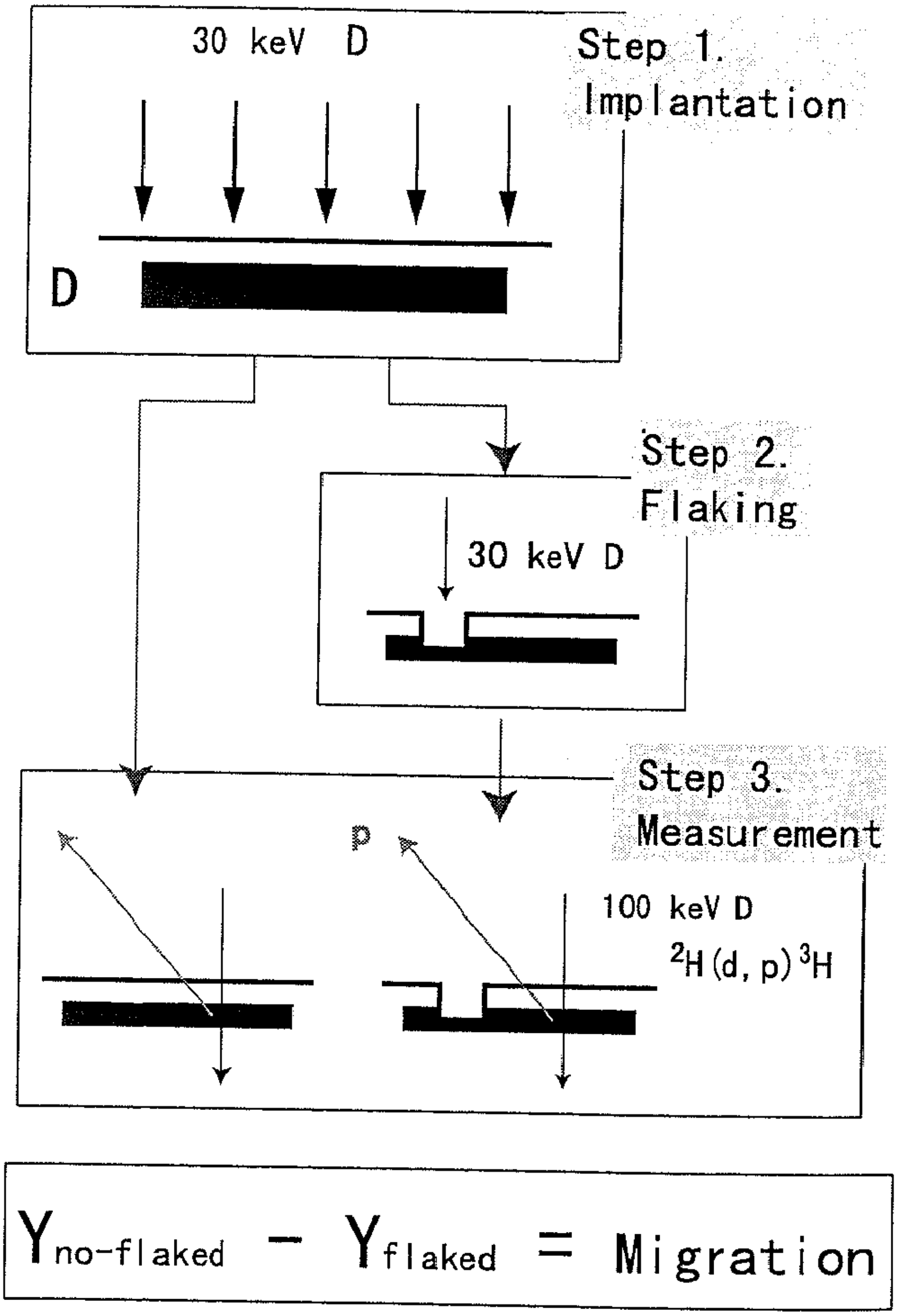

Figure 17: Experiment I: experimental procedure

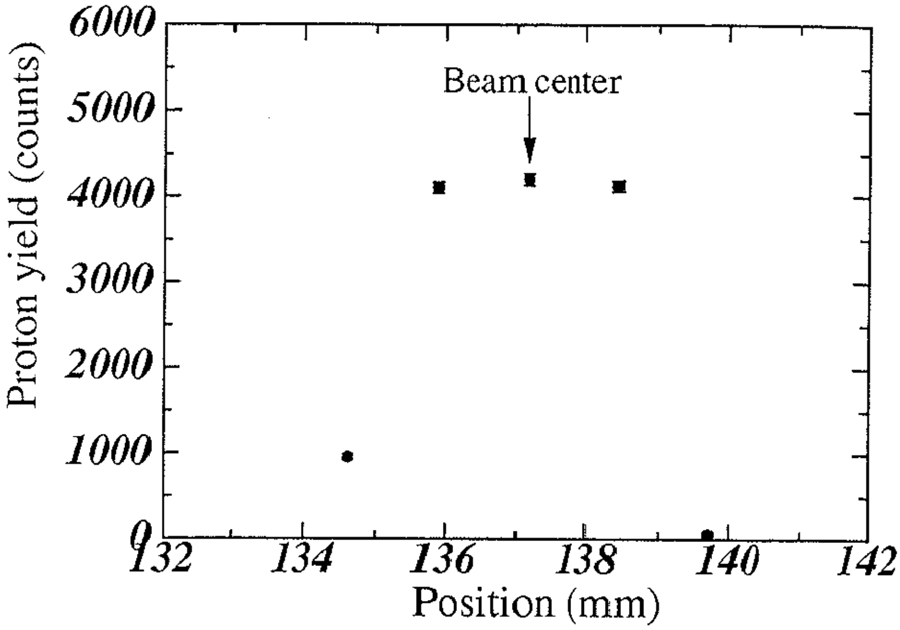

Figure 18: Vertical distribution of implanted deuterium atoms

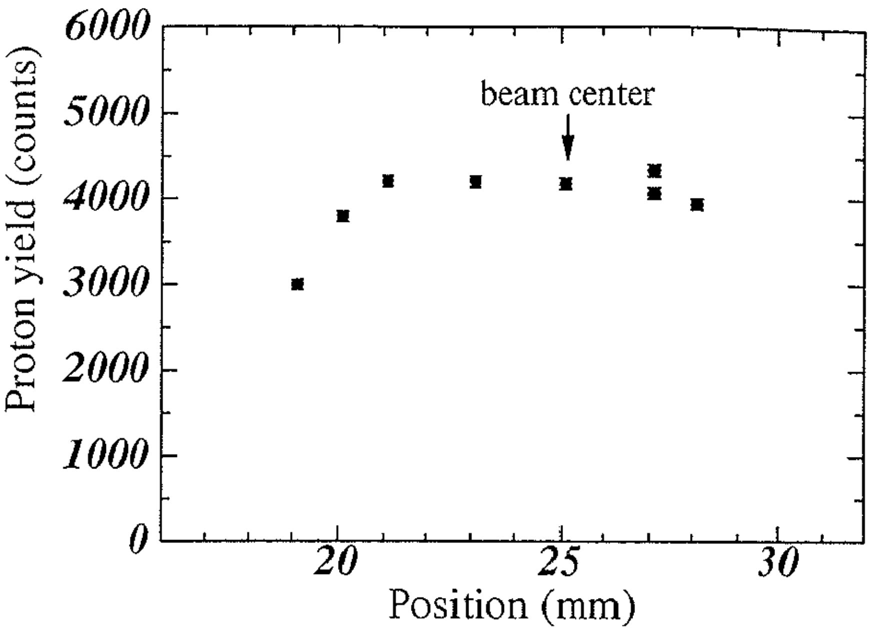

Figure 19: Horizontal distribution of implanted deuterium atoms

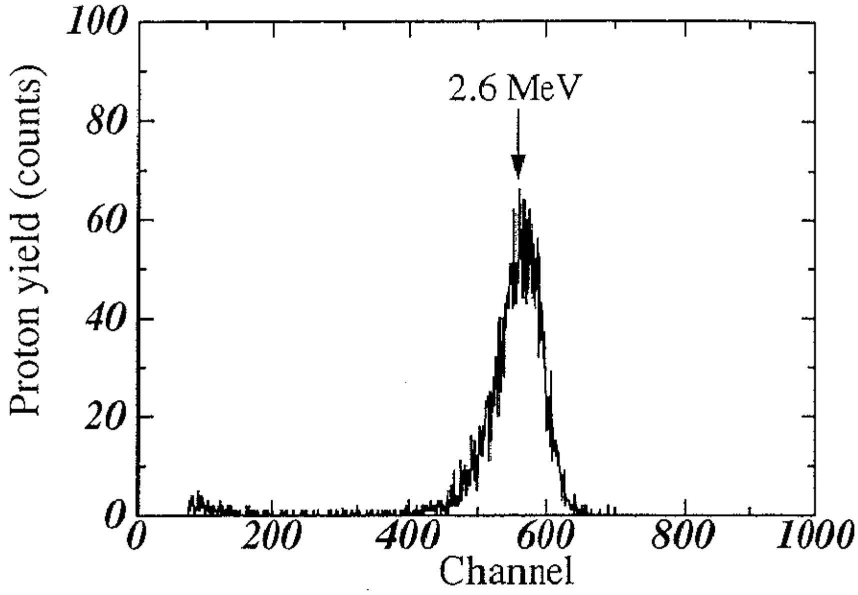

Figure 20: Energy spectrum of the emitted protons from the nuclear reaction $^{2}H(d,p)^{3}H$

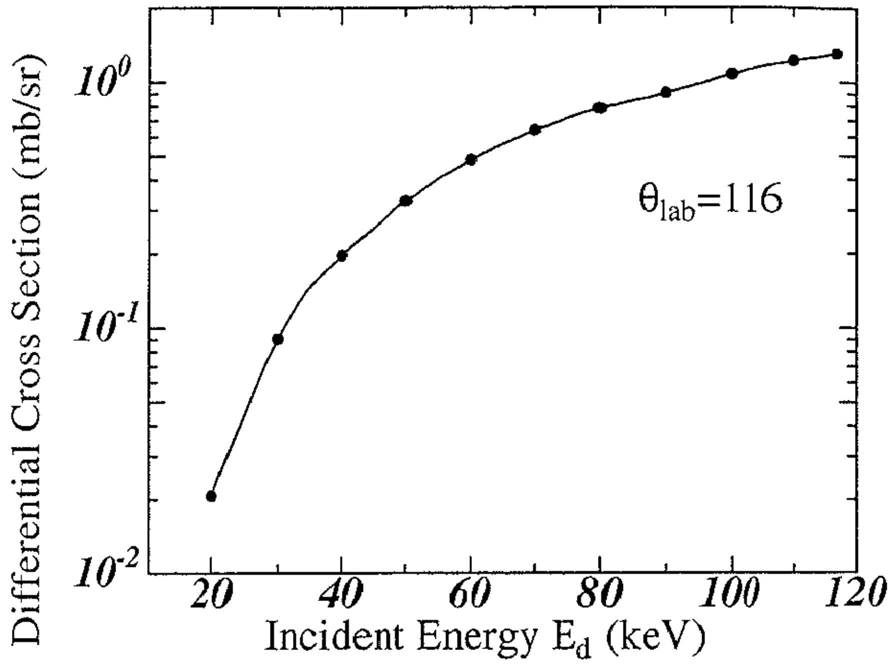

Figure 21: Differential cross section for the nuclear reaction ^{2}H(d,p)^{3}H at an angle of $\theta_{lab} = 116°$ [19]

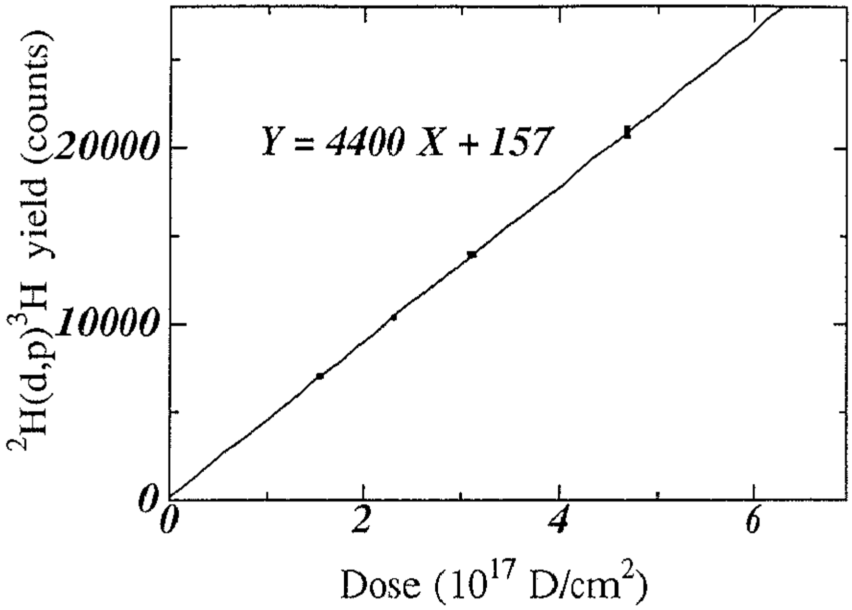

Figure 22: Proton yield for no-flaked samples

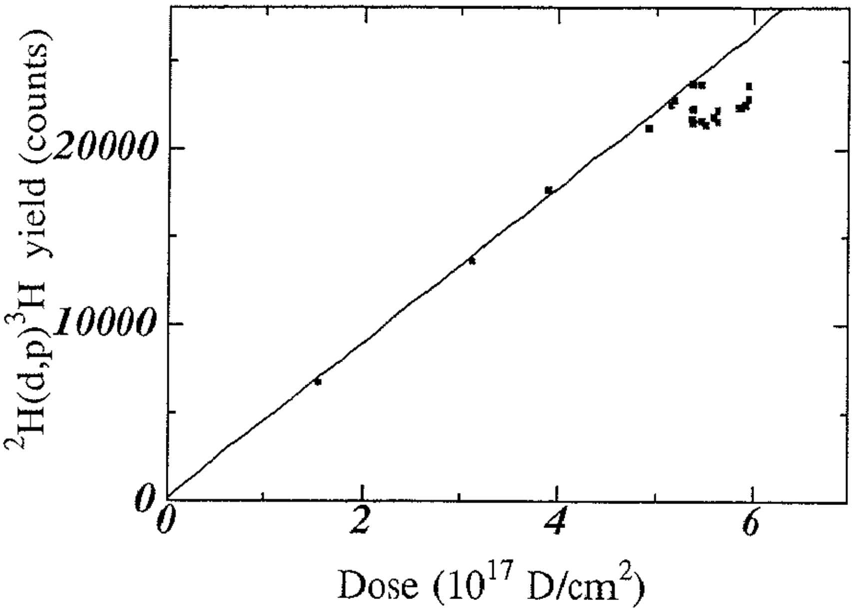

Figure 23: Proton yield for flaked samples

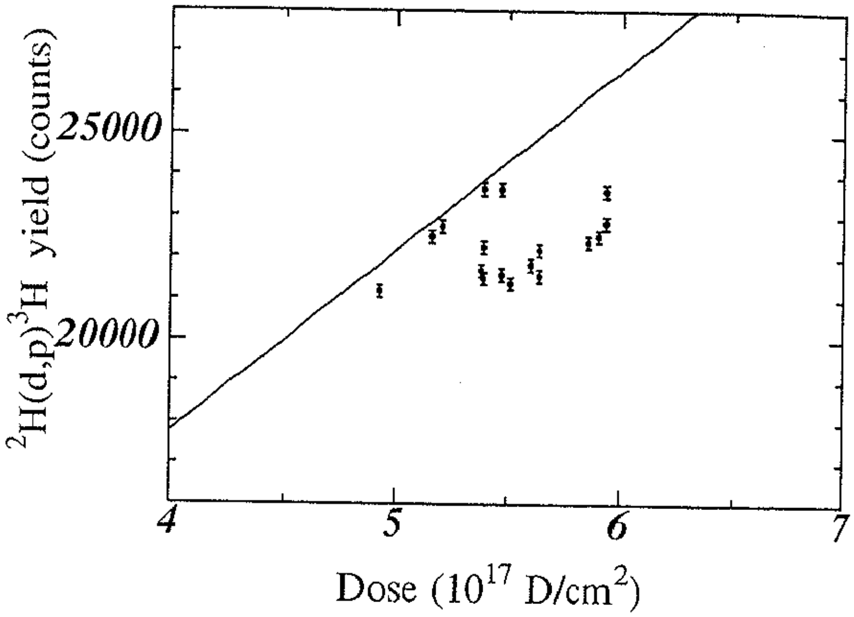

Figure 24: Proton yield in the dose range above 4 × 10^{17} D/cm^2 for flaked samples

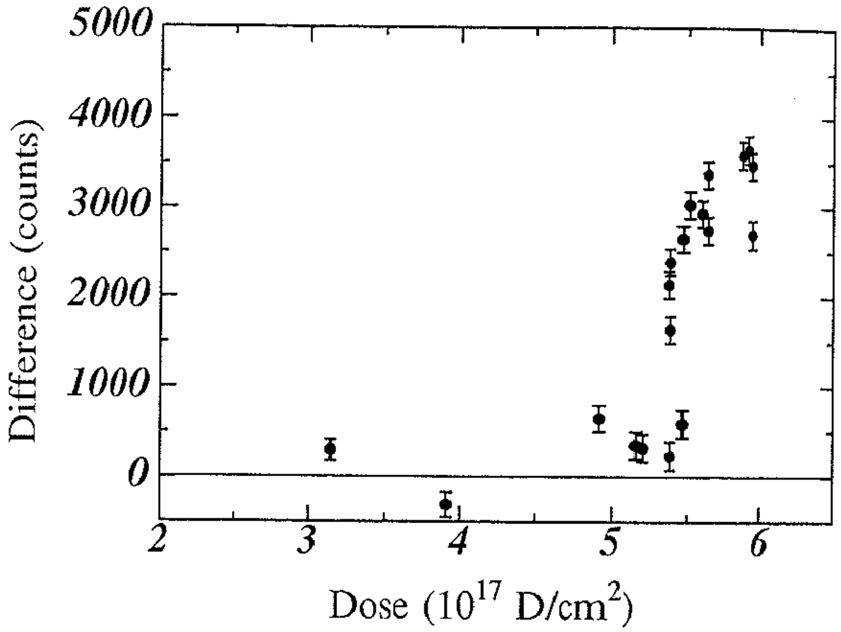

Figure 25: Difference of proton yields between flaked and no-flaked samples

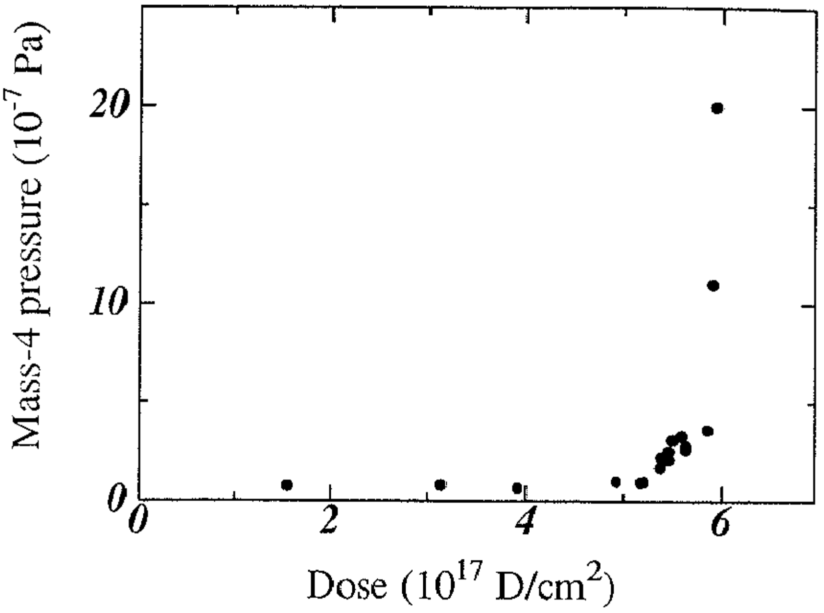

Figure 26: Mass-4 gas partial pressure at the step-2 flaking

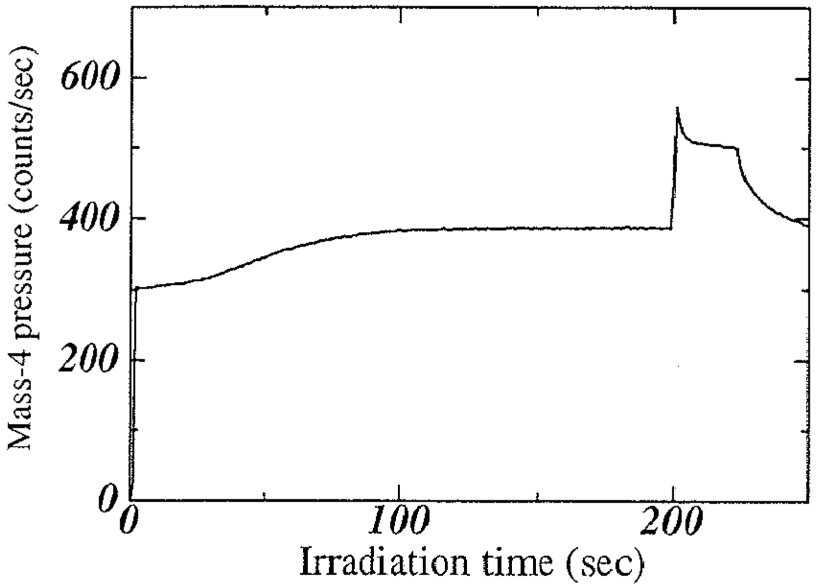

Figure 27: Mass-4 gas partial pressure at flaking for a sample of an implantation dose of 5.9 × 10^{17} D/cm^2

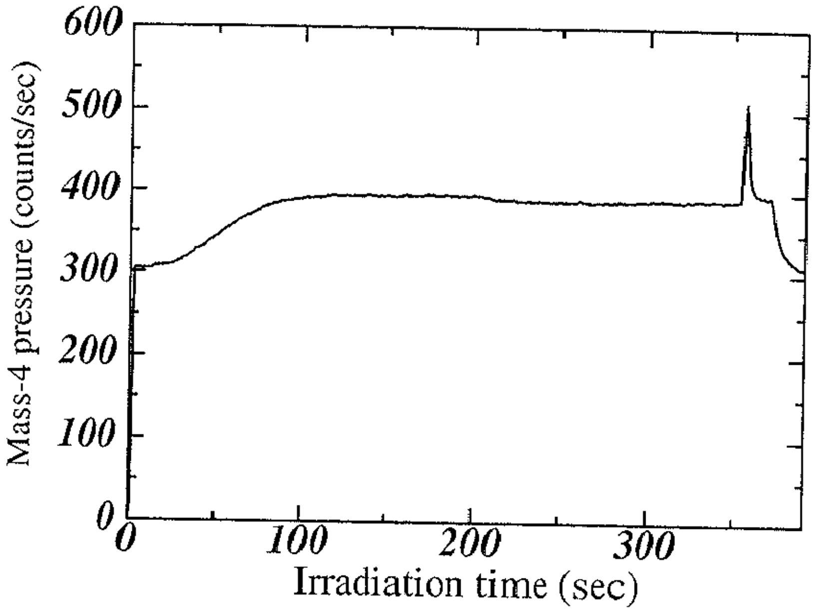

Figure 28: Mass-4 gas partial pressure at flaking for a sample of an implantation dose of 5.4 × 10^{17} D/cm^2

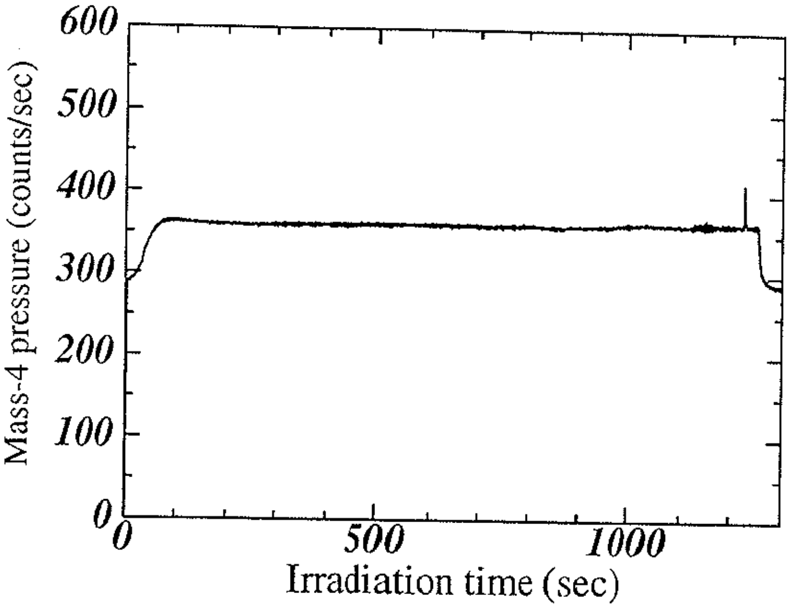

Figure 29: Mass-4 gas partial pressure at flaking for a sample of an implantation dose of 1.6 × 10^{17} D/cm^2

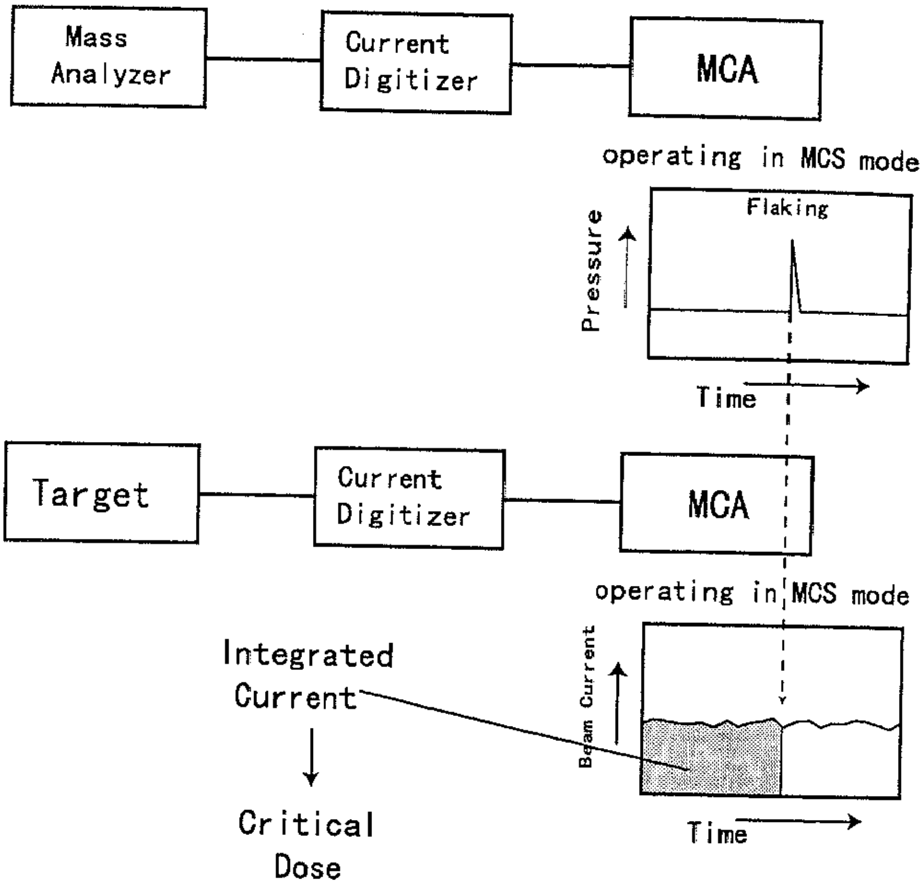

Figure 30: Experimental II: Experimental procedure

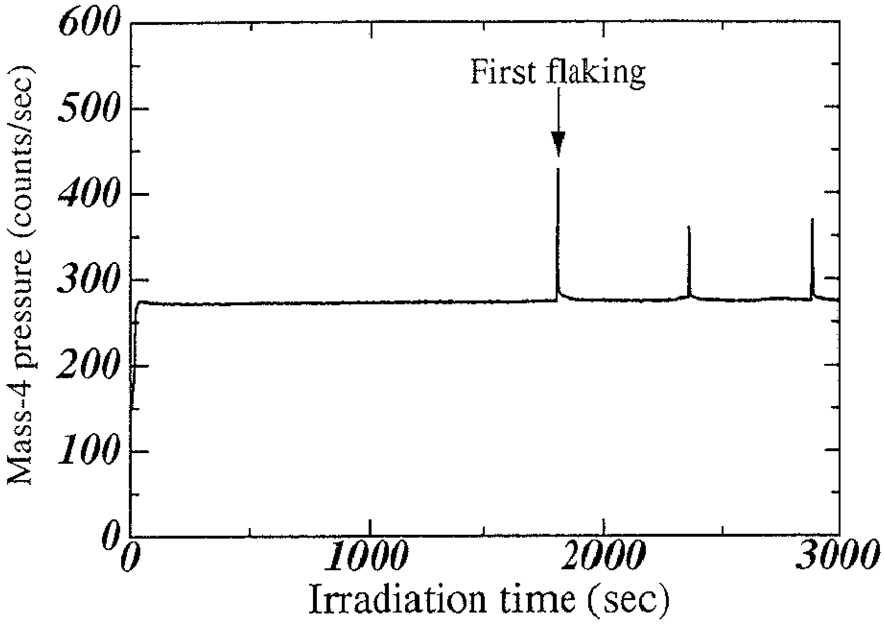

Figure 31: Mass-4 gas pressure for 60-keV D^- irradiation of silicon

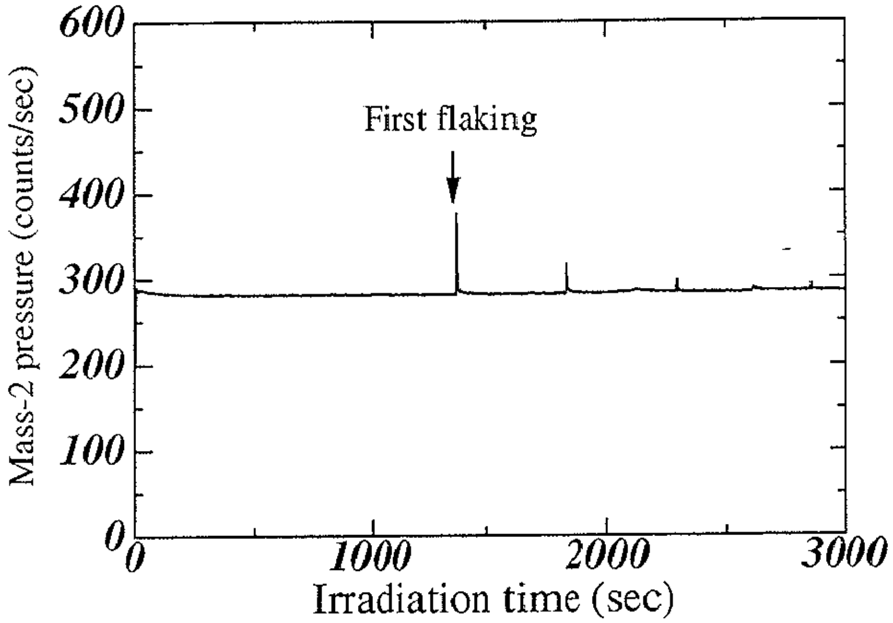

Figure 32: Mass-2 gas pressure for 100-keV H^- irradiation of silicon

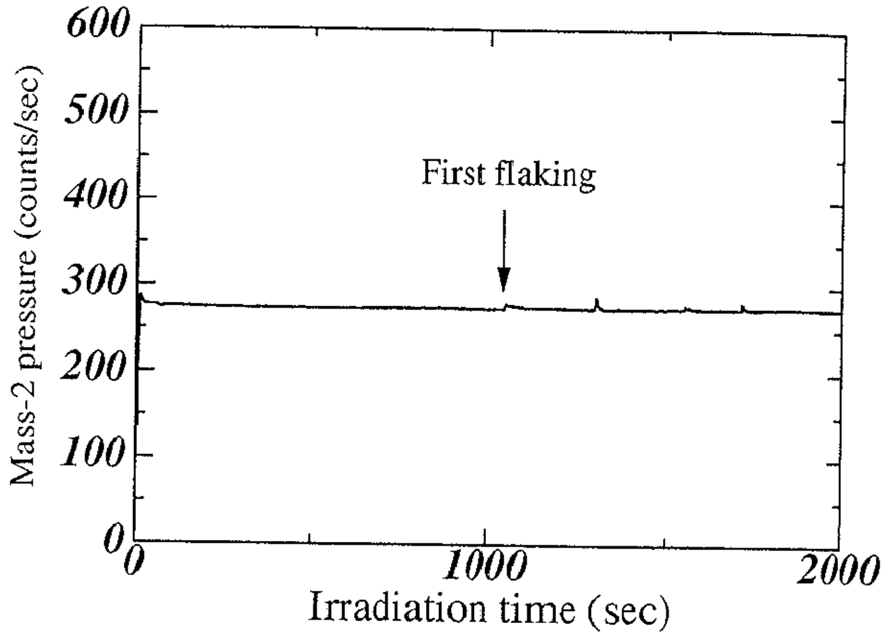

Figure 33: Mass-2 gas pressure for 30-keV H^- irradiation of silicon

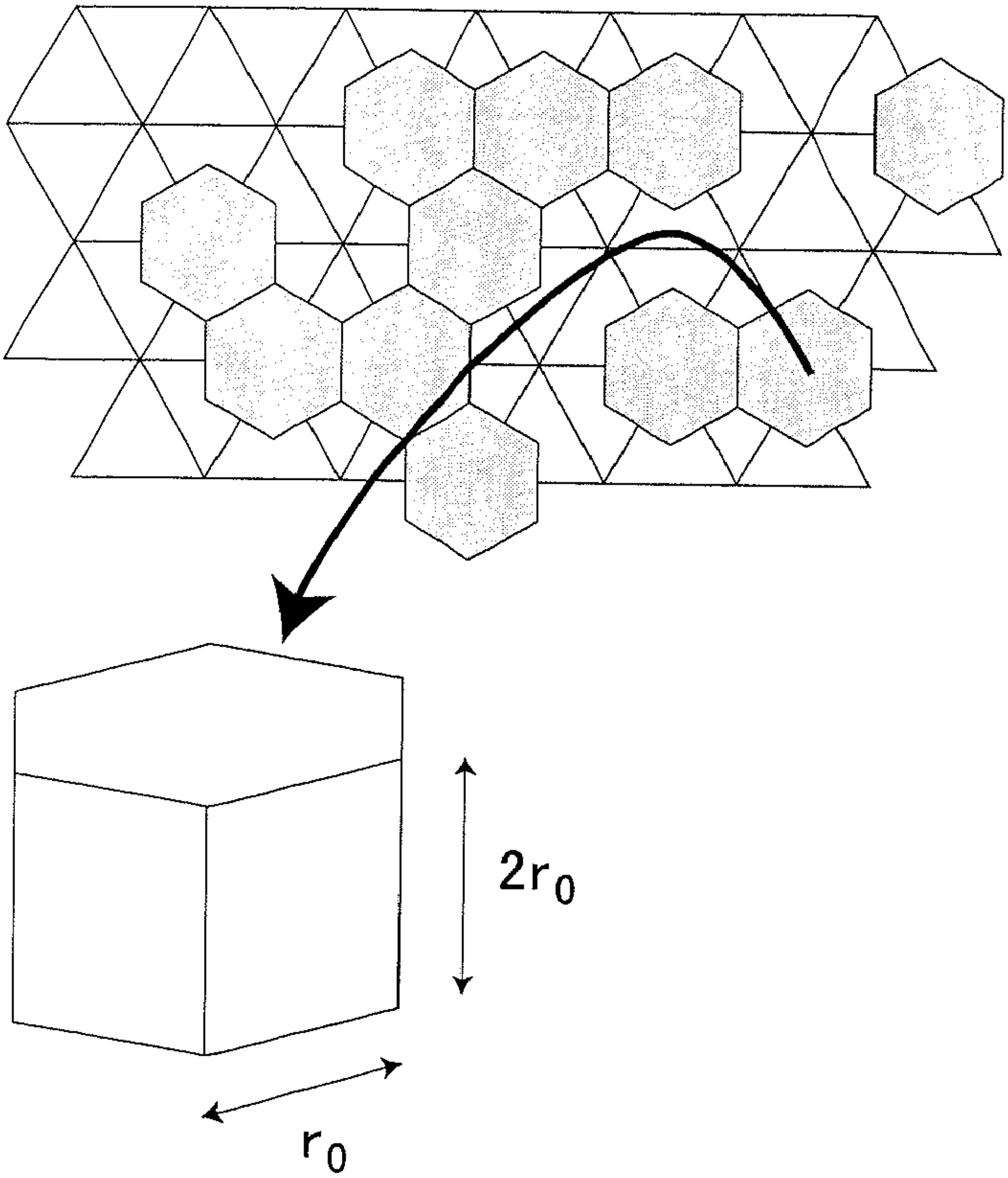

Figure 34: A hexagonal cylinder and a triangular lattice

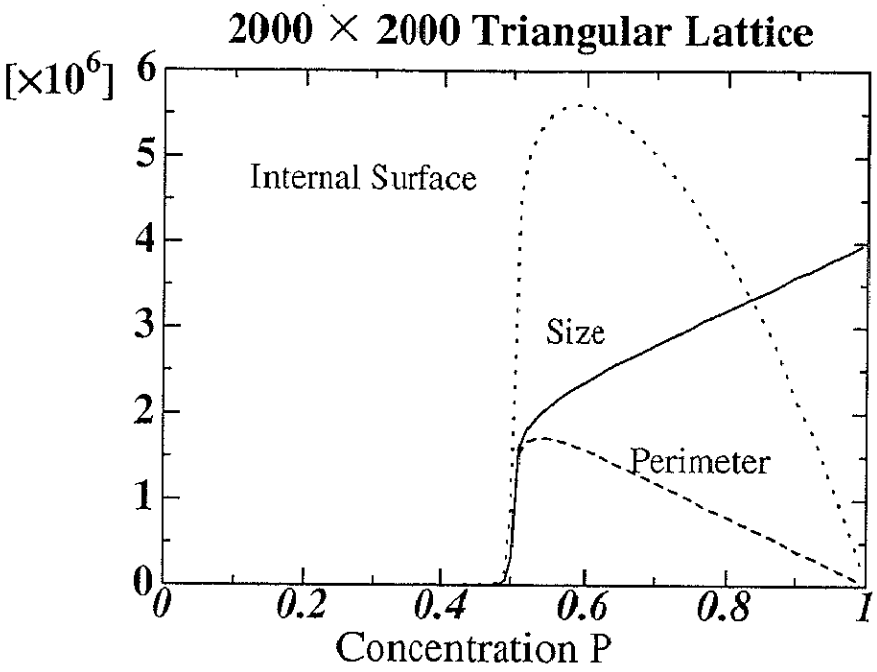

Figure 35: Calculation of 2000 × 2000 triangular lattice

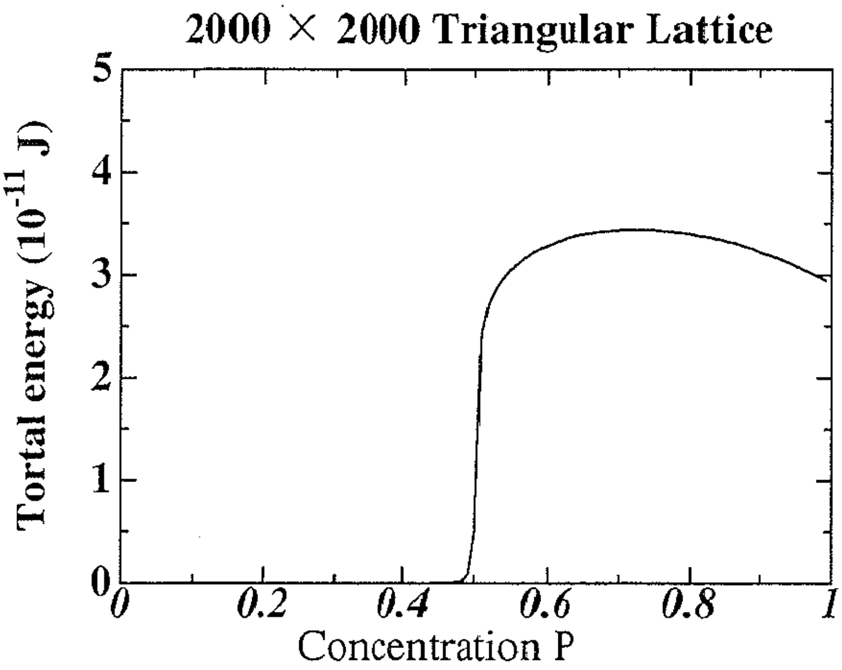

Figure 36: Total energy of triangular lattice

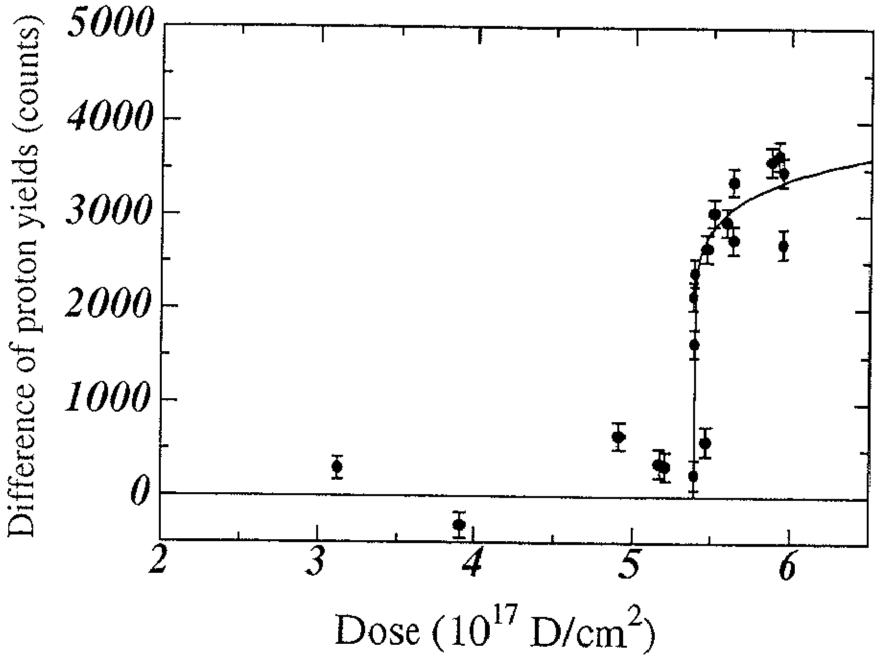

Figure 37: A fitting result (solid curve) and difference of proton yields between flaked samples and no-flaked samples

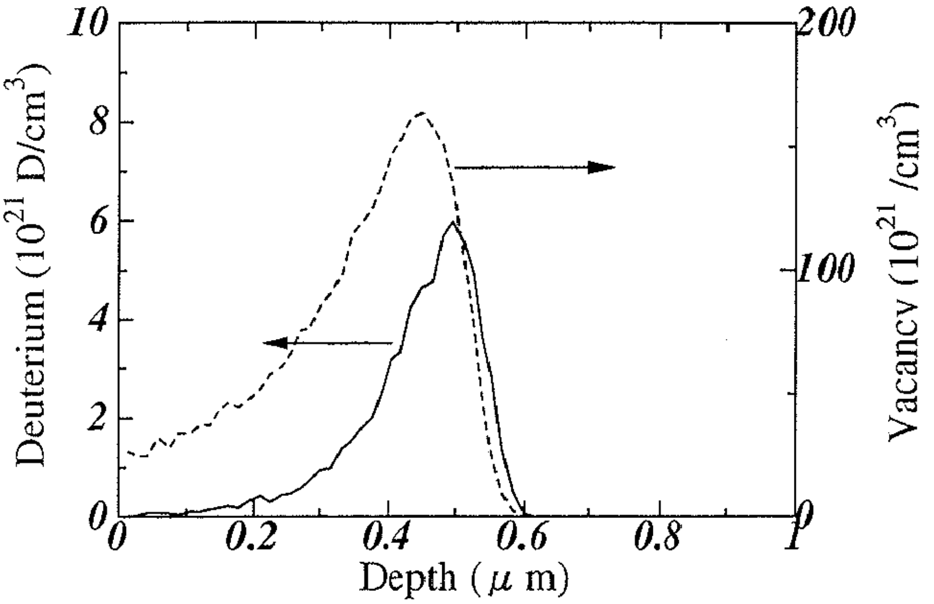

Figure 38: TRIM calculation for 30-keV deuterium implantation into silicon

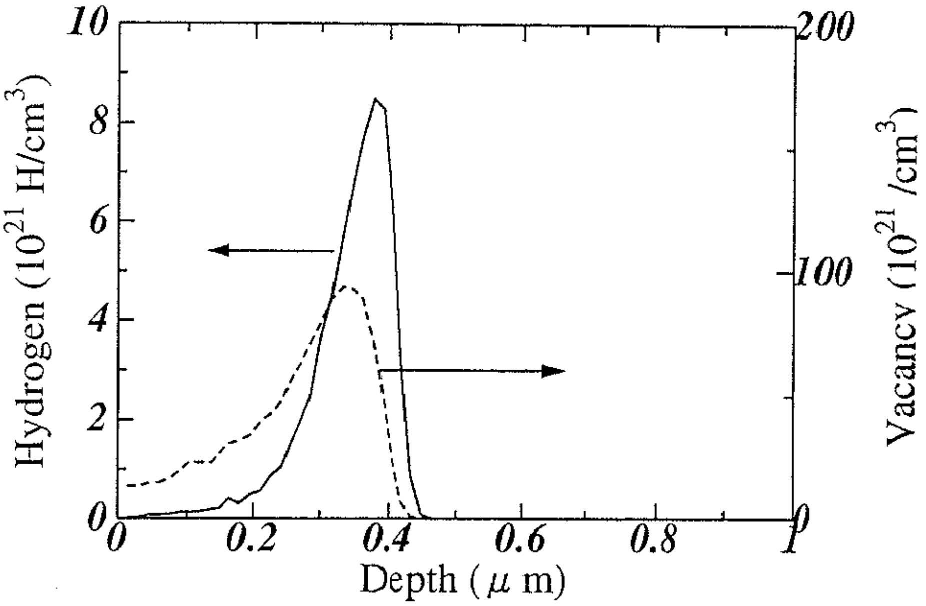

Figure 39: TRIM calculation for 30-kev hydrogen implantation into silicon

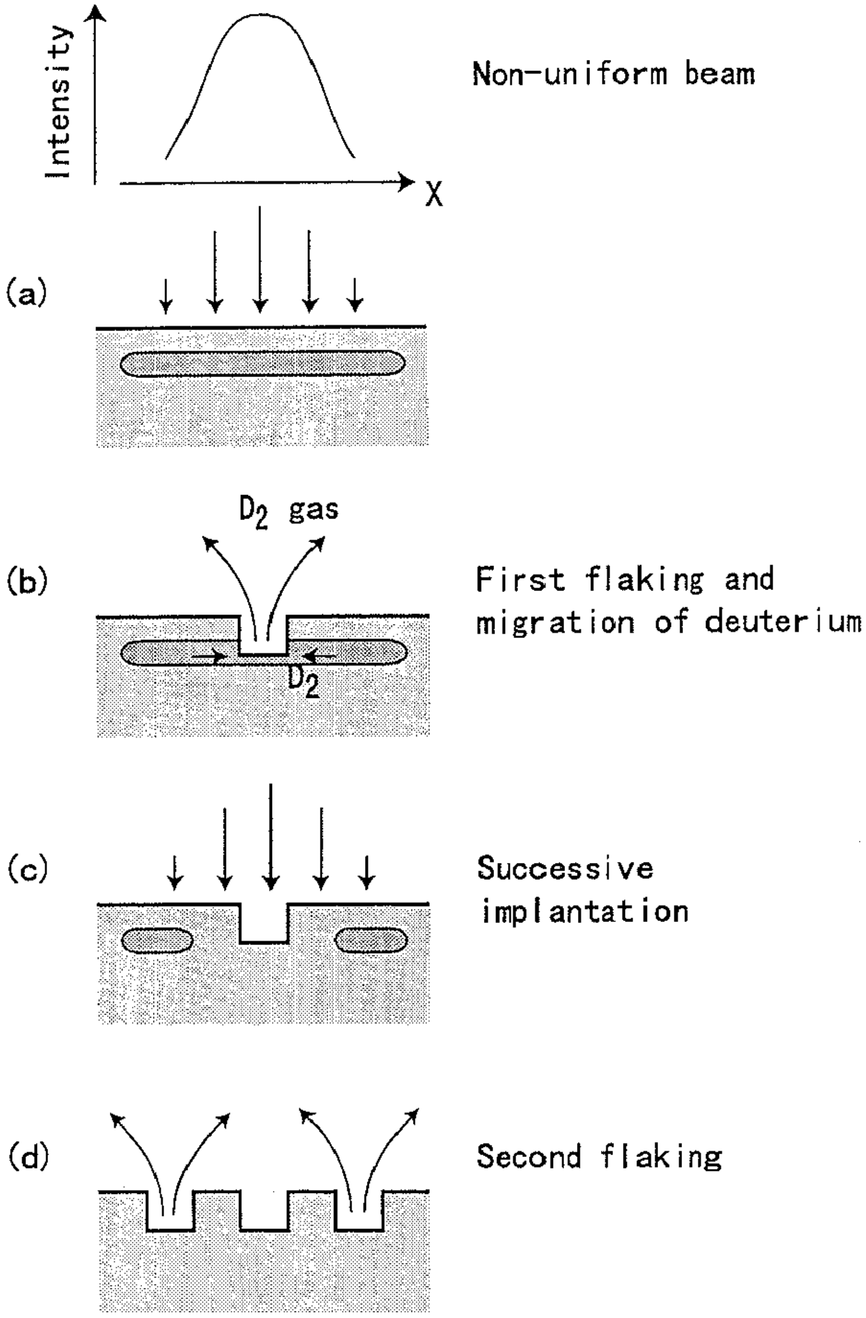

Figure 40: Schematics of formation mechanism of the ring-like flaking craters

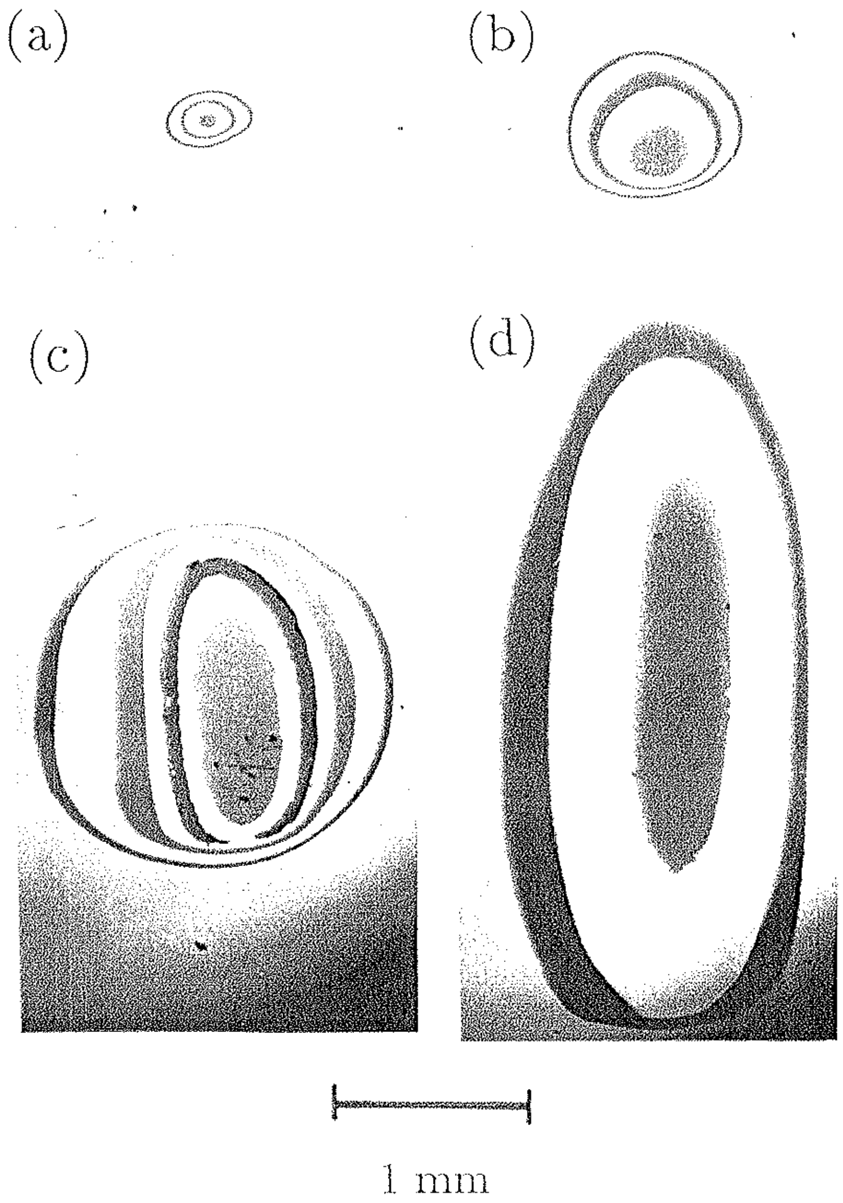

Figure 41: Optical micrographs of the ring-like flaking for various beam sizes. The beam diameter of (a), (b), (c) and (d) is 0.5, 1, 2 and 4 mm, respectively.